DEPARTMENT OF PHYSICS
UNIVERSITY OF JYVÄSKYLÄ
RESEARCH REPORT No. 4/2013

DENSITY FUNCTIONAL / MOLECULAR DYNAMICS SIMULATIONS OF PHASE-CHANGE MATERIALS

BY

JANNE KALIKKA

Academic Dissertation
for the Degree of
Doctor of Philosophy

To be presented, by permission of the
Faculty of Mathematics and Science
of the University of Jyväskylä,
for public examination in Auditorium FYS-1 of the
University of Jyväskylä on March 23rd, 2013
at 12 o'clock noon.

Jyväskylä, Finland
March 2013

Preface

The research for this thesis was done at the Department of physics at the University of Jyväskylä during 2008-2012. The work was financially supported by the Academy of Finland and JST (Japan) under the "Functional Materials" program, and by the faculty of mathematics and science at the University of Jyväskylä. Travel grants from the National Doctoral Programme in Materials Physics are duly acknowledged.

I thank my supervisor, academy research fellow Jaakko Akola for his guidance, and an opportunity to learn much about research over the years. I am very grateful to Dr. R.O. Jones for the collaboration and many discussions throughout my doctoral studies, and also for the critical reading of the thesis manuscript. I also thank the group leader professor Hannu Häkkinen for discussions, and Dr. Vesa Apaja for computer support. I also extend my gratitude to professors Kari Laasonen and Bart Partoens for reviewing the thesis, and professor Jean-Yves Raty for agreeing to be my opponent.

The physics department at the University of Jyväskylä has been an excellent place to study and do research. I'm thankful to all faculty members who have contributed to my learning ever since I started my university studies at Jyväskylä. I feel ready to take a step outside now. I also thank the office personnel who were always ready to help with the practical matters.

Finally, I thank all my friends and family for their support, and giving me something else to think about besides physics and computers. Especially my beloved Reetta, who has encouraged and supported me through delight and despair.

Jyväskylä, March 2013

Janne Kalikka

Abstract

The rapid and reversible phase change in chalcogenide phase-change materials is an unusual property with many technological applications in rewritable optical memory, such as CD, DVD, or Blu-ray Disc. Phase change materials are a promising candidate for next-generation electronic memory applications, and the first devices became available in 2012.

In this thesis, we studied the structure and dynamics of four phase-change materials: $Ge_{15}Te_{85}$, $Ge_2Sb_2Te_5$, GaSb and $GaSb_7$ by simulating the structural models using the density functional (DF) theory of electronic structure. We developed a new model for $Ge_{15}Te_{85}$ by fitting experimental high-energy x-ray and neutron diffraction data with an atomic structure that had a low DF energy. We studied the crystallization progress of $Ge_2Sb_2Te_5$ by simulating the structures with a fixed seed to promote crystallization at 500 K, 600 K and 700 K. In the final article, we used molecular dynamics simulation to mimic deposition of GaSb and $GaSb_7$ thin films and modeled the as-deposited and melt-quenched polymorphs of those alloys.

The new model for $Ge_{15}Te_{85}$ incorporates Ge-Ge bonds, which were excluded from most earlier models. In this material, germanium has two different local environments (tetrahedral and defective octahedral), and tellurium can be classified in two cases depending on its binding with Ge. Nanosized cavities calculated using a Voronoi prescription comprise 22-24% of the total volume.

$Ge_2Sb_2Te_5$ crystallization simulations at different temperatures agreed with the experimental result for the fastest crystallization speed. We show that the crystalline structure has "wrong bonds", which are absent in the idealized model of the structure, and that percolation of the crystalline cluster starts at an early stage of crystallization. Cavities (vacancies) aid the atomic rearrangements during crystallization.

GaSb simulations reveal tetrahedral local coordination for both species, as in crystalline GaSb. This can explain the very fast crystallization speed of this material. In $GaSb_7$, gallium is again bonded tetrahedrally, but antimony has the defective octahedral coordination found in elemental antimony. GaSb has no rings with more than eight atoms but $GaSb_7$ has larger rings. The lack of large rings in GaSb was attributed to the lack of suitable cavities that would allow long irreducible rings to surround them. GaSb structures include Ga-rich clusters similar to the crystalline gallium structure.

Author's address Janne Kalikka
Department of Physics
Nanoscience Center
University of Jyväskylä
P.O. Box 35
FI-40014 University of Jyväskylä
Finland
janne.kalikka@jyu.fi

Supervisor Academy Research Fellow Jaakko Akola
Department of Physics
Tampere University of Technology
Finland

Reviewers Professor Kari Laasonen
Department of Chemistry
Aalto University
Finland

Professor Bart Partoens
Department of Physics
University of Antwerp
Belgium

Opponent Professor Jean-Yves Raty
Department of Physics
University of Liege
Belgium

List of publications

I J. Kalikka, J. Akola, R. O. Jones, S. Kohara and T. Usuki, *Amorphous $Ge_{15}Te_{85}$: density functional high-energy x-ray and neutron diffraction study*, J. Phys.: Condens. Matter **24**, 015802 (2012).

II J. Kalikka, J. Akola, J. Larrucea and R. O. Jones, *Nucleus-driven crystallization of amorphous $Ge_2Sb_2Te_5$: A density functional study*, Phys. Rev. B **86**, 144113 (2012).

III J. Kalikka, J. Akola and R. O. Jones, *Density functional simulations of structure and polymorphism in Ga/Sb films*, J. Phys.: Condens. Matter **25**, 115801 (2013).

The author has done all numerical work in publications I and III and the simulations for the 460-atom models in publication II. He has done the analysis and written the first drafts of all articles. In addition to the publications listed above, the author has contributed to one article and three proceedings publications that are not included in this thesis. These are listed below

- J. Kalikka and J. Akola, *Steered molecular dynamics simulations of ligand-receptor interaction in lipocalins*, Eur. Biophys. J. **40**, 181-194 (2011).
- J. Kalikka, J. Akola, R. O. Jones, S. Kohara and T. Usuki, *Combined density functional and Reverse Monte Carlo simulations of amorphous $Ge_{15}Te_{85}$*, Proc. Europ.\Phase Change and Ovonic Symposium (E*PCOS 2011, Zürich) 195-196 (2011).
- J. Kalikka, J. Akola, J. Larrucea and R. O. Jones, *Crystallization of amorphous $Ge_2Sb_2Te_5$: Order from disorder*, Proc. 10th Intern. Conf. Solid State Chem. 2012 (SSC 2012, Pardubice) 38 (2012).
- J. Kalikka, J. Akola and R. O. Jones, *Computer-aided deposition of Ga_xSb_{1-x} thin films*, Proc. Europ.\Phase Change and Ovonic Symposium (E*PCOS 2012, Tampere) 126-129 (2012).

Contents

Abbreviations

AD	as-deposited (polymorph)
BO	Born-Oppenheimer (approximation)
BO-MD	Born-Oppenheimer Molecular Dynamics
CN	Classical nucleation (theory)
CP-MD	Car-Parrinello Molecular Dynamics
CPMD	The name of the DFT code used in this thesis
DF	Density functional
DOS	Density of states
HK	Hohenberg-Kohn (theorems)
KS	Kohn-Sham (model)
LDA	Local density approximation
MQ	melt-quenched (polymorph)
PBE	Perdew-Burke-Ernzerhof (functional)
PBEsol	Perdew-Burke-Ernzerhof functional for surfaces and solids
PC	Phase-change
PDF	Pair distribution function
RMC	Reverse Monte-Carlo (method)
SE	Schrödinger equation
TF	Thomas-Fermi (model)
TPSS	Tao-Perdew-Staroverov-Scuseria functional

1 Introduction

Humans have a desire to store information. I could start with the dawn of time and cave paintings depicting past events, but instead, I will move to modern times. As of 2007, humans stored approximately 295 exabytes of non-redundant information [1] and the number is growing exponentially. This number is beyond comprehension for an average human, but if this amount of data was stored on state-of-the-art hard disk drives (2 TB capacity, 3.5 in. form factor), those drives could be used to pave an 8-meter-wide road for 243 kilometers, which is almost the distance from Jyväskylä to Helsinki.

An increasing fraction of this information is personal digital photographs or home videos recorded with mobile phones. The data is often kept on these mobile devices. The mobile devices are powered by rechargeable batteries, and it is thus preferred to use memory components with as little need for operating power as possible. Phase-change (PC) memory can be made with low power requirements, and it is the latest addition to the memory types available for consumer electronics.

In PC memory, the information is stored in the atomic structure. This is inherently different from the electric charge used as the fundamental storage medium in DRAM and flash memories, or the magnetization used in hard disk drives. Data recording is done by switching the structure between ordered and disordered phases, and reading utilizes the different electric or optical properties of the phases.

The composition of the material dictates the behavior of the material, e.g. how much operating power it needs or how fast is the data write speed. In addition to varying the ratio of the main constituents, it is possible to affect the behavior of the PC material by doping it with additional elements. Typical dopant concentrations in PC materials are in the few percent range (in contrast to the ppm range used with traditional semiconductors). It is easy to see that the number of possible compositions is very large, and even though there exists some composition-dependent trends in the physical parameters of the materials, there is still much to be discovered.

PC materials are crystalline in the ordered phase, but the disordered amorphous phase has similarities with glassy materials. The most used glassy materials are different compositions of silicate glass, which is mostly SiO_2, and is widely used, for example in windows, or drinking glasses. However, in theory any liquid can be vitrified if cooled fast enough, and even molten metals form so-called bulk metal glasses [2]. Good glass formers vitrify with slower cooling rates when compared to poor glass formers, which require fast cooling rates to avoid crystallization. Glasses in general are rigid, solid materials that do not flow (contrary to the fallacy believed by many, [3]), and are not quite standard solids or liquids. The widespread usage is not based on the fact that we understand the microscopical structure of glasses, which even today is not well-known, and the same can be said about the glass transition[4].

The glass transition, recrystallization, and atomic structure are in the very heart of the operation of PC materials. The reason why PC materials are useful in memory applications is that while they vitrify, the glassy amorphous state is not particularly stable and the material can be readily recrystallized. Thus the fact

that they are poor glass formers is very important for the operation of a memory device, and the fast reversible transition between the two phases is what makes these materials unique. In order to be able to design new PC materials without having to resort to experimental trial-and-error method, it is imperative to shed light on the effect of varying composition on the glassy phase structure and phase transitions. One method which can be used for this is atomistic modeling of the PC material structures and dynamics on a computer.

Computers have been utilized for scientific research for several decades while the computing power has been rapidly increasing. Atomistic simulations have been done since the 1960's but the available computing power restricted the simulations to small clusters, ideal lattices that could be modeled with a few repeating atoms, or systems modeled with classical force fields that do not allow for bond breaking and formation. During the last 10-15 years it has become possible to model systems of a few hundred atoms with methods, such as density functional (DF) theory, which solve the electronic structure and include bond breaking and forming phenomena. These methods are excellent for modeling PC materials, as switching the phase induces significant changes in the bonding network.

This thesis comprises three studies of four PC materials. In the first article, we studied the amorphous structure of $Ge_{15}Te_{85}$, and based on combining experimental data with DF calculations we proposed a new structural model for the material. In the second article, we simulated the crystallization of $Ge_2Sb_2Te_5$ after the formation of critical nucleus, and noted that cavities provide space for the atomic rearrangements during crystallization, and the resulting crystal structure has a number of defects in it. In the final article, we studied different polymorphs of GaSb and $GaSb_7$ PC materials. Here we created models for as-deposited (AD) and melt-quenched (MQ) structures by mimicking the vapor deposition (fabrication) of thin films, and melt-quenching the AD structures into MQ structures. In general, fourfold coordination was present in GaSb for both species, while in $GaSb_7$ gallium was fourfold coordinated and antimony was threefold coordinated. Interesting Ga-rich cluster resembling crystalline gallium was found in the AD structure of GaSb.

The computer simulations presented in this thesis are computationally very demanding and would not have been possible without the vast resources available at the Forschungszentrum Jülich, Germany. For example during the summer of 2012, in two months alone, I used approximately 15 million core-hours of computation time on the new IBM Blue Gene/Q (JuQueen) supercomputer. In terms of floating point operations (FLOP, a measure of the amount of computation), this is equivalent of 207 years of computing on a Core i5 2500 quad-core "Sandy Bridge" desktop computer processor, which was released by Intel in early 2011.

2 Theory

2.1 Density functional theory

2.1.1 Early history

The density functional (DF) theory of electronic structure was developed as a direct consequence to the formulation of quantum mechanics in the early 20th century. Most of this exciting history was brought to my attention by Dr. R.O. Jones [5]. The accurate quantum description of an atom started in 1926 with Erwin Schrödinger's publication of *Quantisierung als Eigenwertproblem* [6], which he later republished in English [7]. These contained a derivation of the Schrödinger Equation (SE). Soon after this it was noted, however, that the exact solution of this equation is impossible for most systems of interest and approximations are needed in order to do calculations. The article, *Quantum Mechanics of Many-Electron Systems*, by P.A.M. Dirac in 1929 starts with the following [8]:

> The general theory of quantum mechanics is now almost complete, the imperfections that still remain being in connection with the exact fitting in of the theory with relativity ideas. These give rise to difficulties only when high-speed particles are involved, and are therefore of no importance in the consideration of atomic and molecular structure and ordinary chemical reactions, in which it is, indeed, usually sufficiently accurate if one neglects relativity variation of mass with velocity and assumes only Coulomb forces between the various electrons and atomic nuclei. The underlying physical laws necessary for the mathematical theory of a large part of physics and the whole of chemistry are thus completely known, and the difficulty is only that the exact application of these laws leads to equations much too complicated to be soluble. It therefore becomes desirable that approximate practical methods of applying quantum mechanics should be developed, which can lead to an explanation of the main features of complex atomic systems without to much computation.

To this day, only one-electron systems such as hydrogenoid atoms or the H_2^+ molecule have been solved analytically [9]. The ability to do almost any kind of numerical calculations on electronic structure is completely due to practical approximations that yield answers close enough to the exact one. Density functional theory is one such practical approximation and today even one of the most used ones.

The density functional theory is conceptually based on the Thomas-Fermi (TF) model [10, 11], which, even though very inaccurate, was the first theory to calculate electronic structure of matter using electron density as the fundamental variable instead of wave functions. Dirac helped to develop the model further by adding an electron exchange term to it in 1930. However the model remained too inaccurate because of the kinetic energy term, which was only exact in the limit of infinite nuclear charge and induced a significant error to the model otherwise. In his paper on the TF model in 1930, Dirac [12] described the fundamental philosophy behind the density functional theory:

> Each three-dimensional wave function will give rise to a certain electric density. This electric density is really a matrix, like all dynamical variables in the quantum theory (although one usually considers only its diagonal elements, as one can insert these directly into one's picture of the atom). By adding the electric densities arising from all the wave functions we can obtain the total electric density for the atom. If we adopt the equations of the self-consistent field as amended for exchange, then this total electric density (the matrix) has one important property, namely, *if the value of the total electric density at any time is given, then its value at any later time is determined by the equations of motion.* This means that the whole state of the atom is completely described simply by this electric density; it is not necessary to specify the individual three-dimensional wave functions that make up the total electric density. Thus one can deal with any number of electrons by working with just one matrix density function.

The italics are in the original. It seemed clear (at least to Dirac) already then, that the electronic density can be used to calculate any property of an atomic system. These two quotations sum up the concept of density functional theory very well. In it, the fundamental variable is the electron density and it is an approximate method to solve problems which have proven impossible for the exact methods. In the following sections I will outline the derivation of density functional theory, explain the differences of different approximations for the exchange-correlation energy and describe pseudopotentials, which are simplifying approximations of the core electrons.

2.1.2 Derivation of density functional theory

There are a number of books and articles [9, 13, 14] where the density functional theory is reviewed and the derivation generally starts from the Hohenberg-Kohn (HK) theorems [15]. The HK theorems are the formal mathematical foundation for working with the electron density instead of the wave functions when calculating energy and other observables. It is important to note that the DF theory is in principle exact, and the only caveat is that the exchange-correlation energy functional E_{xc} is unknown. Thus, in order to calculate anything with DF theory, we need approximations, and different functionals to approximate E_{xc} have been developed over the years with various results. The functionals will be covered in more detail in section 2.2.1.

Starting from Schrödinger equation

$$\hat{H}\Psi = E\Psi \tag{1}$$

with antisymmetric wave function Ψ to satisfy the Pauli principle for interchanging identical fermions, we can write a general Hamiltonian as

$$\hat{H} = -\sum_{I=1}^{P} \frac{\hbar^2}{2M_I} \nabla_I^2 - \sum_{i=1}^{N} \frac{\hbar^2}{2m_\mathrm{e}} \nabla_i^2 + \frac{e^2}{2} \sum_{I=1}^{P} \sum_{J \neq I}^{P} \frac{Z_I Z_J}{\left|\mathbf{R}_I - \mathbf{R}_J\right|} + \frac{e^2}{2} \sum_{i=1}^{N} \sum_{j \neq i}^{N} \frac{1}{\left|\mathbf{r}_i - \mathbf{r}_j\right|} - e^2 \sum_{I=1}^{P} \sum_{i=1}^{N} \frac{Z_I}{|\mathbf{R}_I - \mathbf{r}_i|}, \tag{2}$$

where m_e is the electron mass, M_I and Z_I are the masses and charges of ions, and $\mathbf{R}_I$ and $\mathbf{r}_i$ are the positions of ions and electrons, respectively.

The electronic part of the Hamiltonian $\hat{h}_e$ is

$$\hat{h}_e = -\sum_{i=1}^{N} \frac{\hbar^2}{2m_\mathrm{e}} \nabla_i^2 + \frac{e^2}{2} \sum_{i=1}^{N} \sum_{j \neq i}^{N} \frac{1}{\left|\mathbf{r}_i - \mathbf{r}_j\right|} - e^2 \sum_{I=1}^{P} \sum_{i=1}^{N} \frac{Z_I}{|\mathbf{R}_I - \mathbf{r}_i|} \tag{3}$$

$$= T + V_\mathrm{ee} + V_\mathrm{ext}. \tag{4}$$

This electronic Hamiltonian is usually used to describe the movement of electrons in the potential formed by ions, even though V_ext can in principle be any external potential. In practice when calculating the electronic structure, ions can be regarded as being stationary because of the vast difference of the particle sizes ($M_\mathrm{p} \sim 1836 \times m_\mathrm{e}$). This is called as the Born-Oppenheimer (BO) approximation, or the adiabatic approximation, and it greatly reduces the complexity of the calculations. Because the electronic structure is then solved with stationary ions, the coordinates of the ions are regarded as parameters instead of variables and the potential induced by them is included in V_ext.

The HK theorems require that the electron density $n(\mathbf{r})$ is "*v-representable*", same result was later proven for "*N-representable*" external potential by Levy. *v-representability* requires that there exists a local potential $v(\mathbf{r})$ for which $n(\mathbf{r})$ is a ground-state density, while *N-representability* requires only that the densities are non-negative and integrate to the number of electrons, N [16, 17, 18]. All *v-representable* densities are *N-representable*, but not vice versa.

For any *N-representable* density $n(r)$, Levy proved [16] that for a variational functional

$$F[n] = \min \langle \Psi | T + V_\mathrm{ee} | \Psi \rangle, \tag{5}$$

the ground state energy

$$E_\mathrm{GS} \leq F[n] + \int V_\mathrm{ext}(\mathbf{r})\, n(\mathbf{r})\, \mathrm{d}\mathbf{r}, \tag{6}$$

with the equality holding only for the ground state density, i.e.

$$E_\mathrm{GS} = F[n_\mathrm{GS}] + \int V_\mathrm{ext}(\mathbf{r})\, n_\mathrm{GS}(\mathbf{r})\, \mathrm{d}\mathbf{r}. \tag{7}$$

Based on this we can define our energy functional

$$E[n] \equiv F[n] + \int V_{\text{ext}}(\mathbf{r})\, n(\mathbf{r})\, \mathrm{d}\mathbf{r} \tag{8}$$

$$= T + V_{\text{ee}} + V_{\text{ext}} \tag{9}$$

$$= \hat{h}_e \tag{10}$$

and by minimizing it, we will find the ground state energy of the system. The functional $F[n]$ is not known exactly. If it was, one could use DF theory to calculate electronic energies exactly. The problems when using this method come from the many-body nature of the kinetic energy of interacting electrons T and the electron-electron potential V_{ee}. One could use the TF approximation for the former but that would lead to no molecular bonds or atomic shell structure.

Another approach to approximate the functional $F[n]$ suggested by Kohn and Sham [19] in 1965 was to write the functional as

$$F[n] = T_0[n] + V_{\text{H}}[n] + E_{\text{xc}}[n], \tag{11}$$

where the T_0 is the kinetic energy of non-interacting electrons with the *same* density as the interacting electrons, E_{xc} is the *exchange-correlation* energy and

$$V_{\text{H}}[n] = e^2 \frac{1}{2} \iint \frac{n(\mathbf{r})\, n(\mathbf{r}')}{|\mathbf{r} - \mathbf{r}'|} \mathrm{d}\mathbf{r}\mathrm{d}\mathbf{r}' \tag{12}$$

is the Hartree potential (classical Coulomb potential). The idea is to perform most calculations with much simplier description of a non-interacting system with identical density instead of the true interacting system. This way all many-body effects are moved to the E_{xc}. The other terms can be solved exactly by using single-particle (Kohn-Sham, KS) orbitals $\phi_i(\mathbf{r})$. The density is readily calculated from these orbitals as

$$n(\mathbf{r}) = \sum_{i=1}^{N} \phi_i^*(\mathbf{r})\, \phi_i(\mathbf{r}) \tag{13}$$

and can be used to calculate the $V_{\text{H}}[n]$, T_0 can be written explicitly as

$$T_0 = -\frac{\hbar^2}{2m} \sum_{i}^{N} \int \phi_i^*(\mathbf{r})\, \nabla^2 \phi_i(\mathbf{r})\, \mathrm{d}\mathbf{r} \tag{14}$$

and the only term left is the E_{xc}, for which one needs to find an approximation. The selection of the approximation can affect the resulting energy substantially. There is an extensive comparison of results obtained with different E_{xc} functionals and non-density functional methods in ref. [14].

Effectively, part of T (the correlation kinetic energy $T_{\text{c}} = T - T_0$) and part of V_{ee} (the exchange and correlation potential $V_{\text{xc}} = V_{\text{ee}} - V_{\text{H}}$) are moved to E_{xc} in the

KS scheme. E_{xc} can be further decomposed into exchange and correlation parts, E_{x} and E_{c}, respectively. E_{x} is known as the Fock term and can be written with single-particle orbitals as

$$E_{\mathrm{x}} = -\frac{e^2}{2}\sum_{i}^{N}\sum_{j\neq i}^{N}\frac{\phi_j^*(\mathbf{r})\,\phi_k^*(\mathbf{r}')\,\phi_j(\mathbf{r}')\,\phi_k(\mathbf{r})}{|\mathbf{r}-\mathbf{r}'|}\mathrm{d}\mathbf{r}\mathrm{d}\mathbf{r}'. \tag{15}$$

This way one can write everything, except for the correlation energy, E_{c} in terms of K-S orbitals and not in terms of density directly. In practical applications E_{x} is often approximated along with E_{c}, but a family of functionals (exact exchange functionals) use the exact formulation of E_{x} in eq. 15.

2.2 Practical approximations

We now have formulated the basic theory. As described in the previous chapter, the DF theory would be exact if the exact form of E_{xc} would be known. The first task is to devise an approximation for it. Such approximations are described in the following chapter.

DF theory is usually formulated via KS orbitals in computer simulations. The orbitals are expressed as a linear combination of mutually orthogonal basis functions. The group of basis functions is called as a basis set, and there are multiple ways to define one. In atom or molecular calculations a good choice would be atom-centered orbital basis, but as the calculations in this thesis involve solids a plane-wave basis is used. Plane-wave basis and the accompanying pseudopotentials are described in the section 2.2.2.

We need to solve some practical matters for numerical calculations to be able to calculate a ground-state energy of an electronic system on a computer. In practical calculations the energy is calculated as follows. The exchange-correlation potential is defined as

$$\mu_{\mathrm{xc}}[n(\mathbf{r})] = \frac{\delta E_{\mathrm{xc}}[n(\mathbf{r})]}{\delta n(\mathbf{r})} = \frac{E_{\mathrm{xc}}[n(\mathbf{r})+\delta n(\mathbf{r})] - E_{\mathrm{xc}}[n(\mathbf{r})]}{\delta n(\mathbf{r})}, \tag{16}$$

where $\delta n(\mathbf{r})$ is a small variation in the density. The single-particle eigenvalue equation is

$$\left[-\frac{\hbar^2}{2m}\nabla^2 + V_{\mathrm{H}} + V_{\mathrm{ext}} + \mu_{\mathrm{xc}}\right]\phi_i(\mathbf{r}) = \epsilon_i\phi_i(\mathbf{r}), \tag{17}$$

and we recall the density from eq. (13). These are then solved self-consistently with a computer by calculating $n(\mathbf{r})$ from initial guess orbitals, using the result to calculate $\mu_{\mathrm{xc}}[n(\mathbf{r})]$ and subsequently solving the eigenvalue problem. However the orbitals $\phi(\mathbf{r})$ vary with the density, i.e. $\phi[n(\mathbf{r})]$, and thus, one can calculate the new density $n_{\mathrm{new}}(\mathbf{r})$ using

$$n_{\text{new}}(\mathbf{r}) = \sum_{i=1}^{N} \phi_i^* [n_{\text{old}}](\mathbf{r}) \phi_i [n_{\text{old}}](\mathbf{r}). \tag{18}$$

The new and old densities, n_{new} and n_{old}, should be the same. In practice, they are not and this self-consistent loop is carried on until the difference is below a convergence threshold defined by the user. There are various mixing schemes developed to speed up the convergence (via damping the oscillations from old to new density), where the new density is not used "as is" but is mixed with the old density instead. A simple mixing scheme is to use a fraction of the n_{old} in addition to the orbitals calculated using it

$$n_{\text{new}}(\mathbf{r}) = \alpha \sum_{i=1}^{N} \phi_i^* [n_{\text{old}}](\mathbf{r}) \phi_i [n_{\text{old}}](\mathbf{r}) + (1-\alpha) n_{\text{old}}(\mathbf{r}). \tag{19}$$

More details of various mixing schemes are described for example in ref. [9].

2.2.1 Approximations of the exchange-correlation energy

Various approximations for the E_{xc} functional have been developed over the years. Typically, they are referred to simply as "functionals", and a common question among the experts of the field is "Which functional did you use?". Over the years, several tens of functionals have been developed, and in 2001 John Perdew presented an elegant way to arrange them in families on rungs of a "Jacob's ladder" that is shown in figure 1. On the rungs are the functional families (right) and each step adds a new quantity (left) on which the energy functional of that rung depends on in addition to the dependencies of the previous rungs. However, the added dependencies make the functionals require progressively more computation. It is also worth noting that adding more sophisticated dependencies to the functional form does not automatically make it more accurate. The most accurate functional tends to depend on the system which one is calculating, and the best functional for one calculation might be outperformed by another one in a different calculation [20].

The bottom rung is the local density approximation (LDA), where the exchange-correlation energy is approximated with that of the homogeneous electron gas (HEG) of equal density. The exchange part of this can be derived analytically but correlation part requires, for example quantum Monte Carlo simulations. The energy can be written as

$$E_{\text{xc}}^{\text{LDA}} = \int n(\mathbf{r}) \epsilon_{\text{xc}}^{\text{H}}[n(\mathbf{r})] \mathrm{d}\mathbf{r}, \tag{20}$$

where the $\epsilon_{\text{xc}}^{\text{H}}[n(\mathbf{r})]$ is the exchange-correlation energy per electron in HEG with density n. In the LDA calculation this is a function of $\mathbf{r}$ regardless of the HEG density itself being homogeneous, because within LDA the density varies, and it is assumed *separately* for each $\mathbf{r}$ that $\epsilon_{\text{xc}}^{\text{H}} = \epsilon_{\text{xc}}^{\text{H}}[n(\mathbf{r})]$.

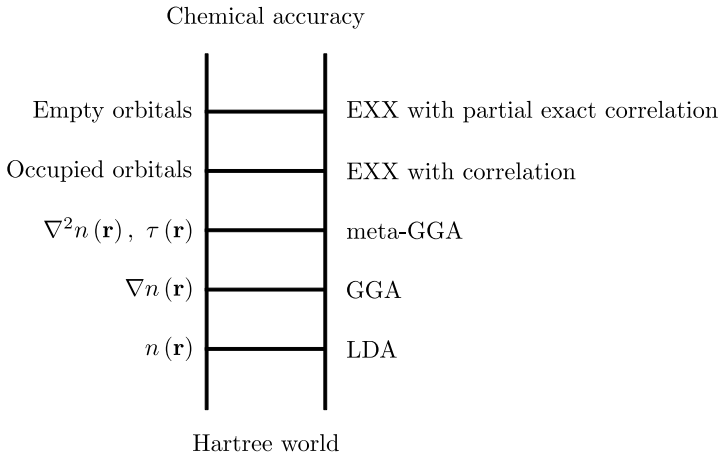

Figure 1: Jacob's ladder of approximations for exchange-correlation energy functional after J.P. Perdew [21].

The next rung is the generalized gradient expansion (GGA) functionals. In addition to the value of density in each point $\mathbf{r}$ they incorporate the rate of change of the density, ∇n. In a sense, LDA can be regarded as using zeroth-order approximation and GGA as the first-order approximation of the density profile. A general GGA functional form can be written as

$$E_{\mathrm{xc}}^{\mathrm{GGA}} = \int n(\mathbf{r}) f[n(\mathbf{r}), \nabla n(\mathbf{r})] \mathrm{d}\mathbf{r}. \tag{21}$$

At this stage the number of possibilities for different functionals increases greatly. The LDA is in principle unique with possibly different parametrizations but in the GGA world there is no perfect way to define a functional.

One GGA functional is known as the Perdew-Burke-Ernzerhof (PBE) functional [22]. As a non-empiciral functional it has no adjustable parameters other than those of the LDA part, and it is the basis for another functional tailored specifically for surfaces and solids (PBEsol) [23], which in turn was used for most calculations of this thesis. Another widely used GGA functional is the BLYP functional [24], which combines Becke's exchange functional (B) [25] and Lee-Yang-Parr (LYP) correlation functionals [26]. B and LYP functionals (and thus also BLYP) differ from other commonly used functionals by being derived from short-range two-particle effects instead of electron gas properties [24]. It is important to note that on the GGA level it is impossible to construct a functional that would give accurate molecular dissociation energies as well as accurate energies for densely packed solids and their surfaces [23]. This is one more reason why there are so many functionals. Naturally, one needs to choose a good functional for the system one is calculating.

The third rung includes meta-GGA functionals that include the orbital-dependent kinetic energy

$$\tau(\mathbf{r}) = \frac{\hbar^2}{2m} \sum_i^{\text{occ}} \left|\nabla \phi_i(\mathbf{r})\right|^2 \tag{22}$$

or the second derivative of the density ($\nabla^2 n$)

$$E_{\text{xc}}^{\text{mGGA}} = \int n(\mathbf{r}) f[n(\mathbf{r}), \nabla n(\mathbf{r}), \tau(\mathbf{r})] \mathrm{d}\mathbf{r}. \tag{23}$$

In addition to PBEsol, the other functional used in this thesis is the Tao-Perdew-Staroverov-Scuseria (TPSS) functional [27], and it is an example of this rung and functional family. While these functionals are not true orbital functionals, they contain an orbital-dependent term (τ).

The last two rungs are occupied by hybrid functionals which utilize the exact exchange (EXX) representation (Eq. 15) of the exchange part of E_{xc} and calculate the correlation part in various ways. These functionals are directly dependent on the orbitals, either only occupied orbitals or both occupied and unoccupied orbitals. Hybrid functionals are typically functionals that have combined the exchange and correlation energies from multiple methods. These can include the EXX with a weight factor. For example, the B3 functional [28] combines the local spin-density approximation (LSDA), EXX, the B88 functional [25] and PW91 functional [29] with three (hence the name) empirically fitted weight coefficients, and B3LYP [30] combines the B3 and LYP functionals (using VWN local correlation [31]). The Heyd-Scuseria-Ernzerhof (HSE) functional [32] is an example of a hybrid functional that weights computation speed in its design. HSE uses PBE0 [33], a hybrid functional by Perdew, Burke and Ernzerhof based on PBE, and utilizes Coulomb screening to speed up calculations in metallic solids and large molecules.

Functionals on all rungs have also corresponding spin-polarized versions, which are actually the ones more commonly in use. In these, the density n is divided into spin-up and spin-down densities that sum up to the total density $n(\mathbf{r}) = n_\uparrow(\mathbf{r}) + n_\downarrow(\mathbf{r})$ and the corresponding terms are explicitly dependent on the up and down spin densities: $\epsilon_{\text{xc}}^{\text{H}}[n(\mathbf{r})] \Rightarrow \epsilon_{\text{xc}}^{\text{H}}[n_\uparrow(\mathbf{r}), n_\downarrow(\mathbf{r})]$ and $f[n(\mathbf{r}), \nabla n(\mathbf{r}), \tau(\mathbf{r})] \Rightarrow f[n_\uparrow(\mathbf{r}), n_\downarrow(\mathbf{r}), \nabla n_\uparrow(\mathbf{r}), \nabla n_\downarrow(\mathbf{r}), \tau_\uparrow(\mathbf{r}), \tau_\downarrow(\mathbf{r})]$.

2.2.2 Plane-wave method and pseudopotentials

Plane-wave basis set consists of plane waves with different energies up to a cutoff energy, which is defined in the simulation parameters. A higher cutoff energy means more individual plane-waves and increased cost of computation. In principle, this cutoff should be very high because of the sharply-peaking potential of the atomic nuclei which require similarly-shaped waves (high energy means short wave length and thus steep oscillation) to approximate wave functions across the nuclei regions. This requirement can be alleviated by the usage of pseudopotentials which replace the core electron states and the nucleic charge with a unified potential. This potential is less steep than pure nucleic potential, and this makes it possible to achieve good accuracy with lower energy cutoff for plane-waves.

The pseudopotentials used in this thesis are norm-conserving and scalar-relativistic Troullier-Martins pseudopotentials [34]. In their paper, they list four criterion that most pseudo-potentials satisfy. First, the valence pseudo-wave-function generated from the pseudo-potential should contain no nodes. Second, pseudo-wave-function and all-electron wave functions are equal beyond a suitable l-dependent cutoff radius r_{cl}. Third, total charge within a sphere with radius r_{cl} are equal. This is the norm-conserving condition

$$\int_0^{r_c} \left| rR_l^{\mathrm{PP}}(r) \right|^2 \mathrm{d}r = \int_0^{r_c} \left| rR_l^{\mathrm{AE}}(r) \right|^2 \mathrm{d}r, \tag{24}$$

where R_l^{PP} and R_l^{AE} are the pseudo-wave function and the all-electron wave function, respectively. And fourth, valence all-electron and pseudopotential eigenvalues must be equal.

Troullier and Martins prescribe a recipe for a pseudopotential, where a radial SE

$$\left(-\frac{1}{2}\frac{\mathrm{d}^2}{\mathrm{d}r^2} + \frac{l(l+1)}{2r^2} + V[\rho; r] \right) rR_{ln}(r) = \epsilon_{nl} rR_{nl}(r) \tag{25}$$

is inverted to solve the screened pseudopotential

$$V_{\mathrm{scr},\,l}^{\mathrm{PP}}(r) = \epsilon_l - \frac{l(l+1)}{2r^2} + \frac{1}{2rR_l^{\mathrm{PP}}(r)} \frac{\mathrm{d}^2}{\mathrm{d}r^2} \left[rR_l^{\mathrm{PP}}(r) \right], \tag{26}$$

$V[\rho; r]$ is self-consistent one-electron potential. The ionic pseudopotential is then calculated as

$$V_{\mathrm{ion},\,l}^{\mathrm{PP}}(r) = V_{\mathrm{scr},\,l}^{\mathrm{PP}}(r) - V_{\mathrm{H}}^{\mathrm{PP}}(r) - V_{\mathrm{xc}}^{\mathrm{PP}}(r), \tag{27}$$

by subtracting the Hartree $V_{\mathrm{H}}^{\mathrm{PP}}(r)$ and exchange-correlation $V_{\mathrm{xc}}^{\mathrm{PP}}(r)$ potentials from the screened potential. This yields a pseudopotential which has a separate l-dependent potential acting on each angular momentum component of the wave function. The ionic pseudopotential operator is defined as

$$\hat{V}_{\mathrm{ion}}^{\mathrm{PP}}(r) = V_{\mathrm{ion,\,local}}^{\mathrm{PP}}(r) + \sum_l V_{\mathrm{nonlocal},\,l}(r)\, \hat{P}_l, \tag{28}$$

where $V_{\mathrm{ion,\,local}}^{\mathrm{PP}}(r)$ is the local potential and

$$V_{\mathrm{nonlocal},\,l}(r) = V_{\mathrm{ion},\,l}^{\mathrm{PP}}(r) - V_{\mathrm{ion,\,local}}^{\mathrm{PP}}(r) \tag{29}$$

is the semilocal potential for each l and $\hat{P}_l$ is the projection operator of the angular momentum component l. The semilocal potential can be written as

$$V^{\mathrm{KB}}_{\mathrm{nonlocal},\,l}(r) = \frac{\left|V_{\mathrm{nonlocal},\,l}(r)\,\Phi^{\mathrm{PP},\,0}_{l}(r)\right\rangle \left\langle \Phi^{\mathrm{PP},\,0}_{l}(r)\,V_{\mathrm{nonlocal},\,l}(r)\right|}{\left\langle \Phi^{\mathrm{PP},\,0}_{l}(r)\right| V_{\mathrm{nonlocal},\,l}(r)\left|\Phi^{\mathrm{PP},\,0}_{l}(r)\right\rangle} \tag{30}$$

following Kleinman and Bylander (KB) [35]. Here the $\Phi^{\mathrm{PP},\,0}_{l}(r)$ is the atomic reference pseudo-wave-function that includes the l-component for which the pseudopotential was calculated. This separable form of the potential greatly reduces the computation when calculating electron structures.

One last property affecting the computational cost is the smoothness of the pseudopotential. The term smoothness refers to the convergence rate of the calculation in this context – calculations using smoother pseudopotentials converge faster in terms of the required plane waves in the basis set. One way to create smooth pseudopotentials, referred to by Troullier and Martins as their "favorite recipe", is the following. The functional form of the pseudo-wave-function is

$$R^{\mathrm{PP}}_{l}(r) = r^{l}\exp\left[p(r)\right], \tag{31}$$

where

$$p(r) = c_0 + c_2 r^2 + c_4 r^4 + c_6 r^6 + c_8 r^8 + c_{10} r^{10} + c_{12} r^{12} \tag{32}$$

with $r \leq r_c$, which is the cutoff radius for the pseudopotential. At higher radii, the all-electron wave function is used. This formulation yields a pseudopotential which, in addition to conforming to the four criterion listed above, is very smooth at the origin because the polynomial contains only even powers of $\mathbf{r}$.

The coefficients c are determined with seven conditions which are listed in the original paper. These are norm-conservation requirement, five continuity-conditions of the polynomial and its first four radial derivatives at r_c to make the transition from pseudo-wave-function to all-electron wave function smooth, and a zero-curvature condition for the screened pseudopotential at the origin to allow the use of smaller energy cutoff for the plane-wave basis. Finally, scalar-relativistic pseudopotentials take into account the fact that innermost core electrons in heavy atoms have such high energies that relativistic corrections are required. This is the case for the chalcogenide alloys in this thesis.

3 Methods

3.1 CPMD software package

CPMD [36] is a parallel simulation code, which specializes in density-functional / molecular dynamics (DF/MD) simulations with plane-waves and uses pseudopotentials. CPMD can be used for Car-Parrinello molecular dynamics (CP-MD) as well as Born-Oppenheimer molecular dynamics (BO-MD) calculations, and both methods were used in the present work. The code also supports various geometry optimization methods. The calculations are parallelized over the 3D Fourier transform grid points (in one of the dimensions) and by the use of distributed linear algebra. The former results in good "soft scaling" of the code, which means the scaling when problem size is increased with the number of processors. This makes it possible to efficiently increase system size while increasing the number of processors.

3.2 Molecular dynamics calculation methods, BO-MD and CP-MD

In the present work, two different molecular dynamics methods were used. Both are based on electronic structure calculations with the DF theory, and they are sometimes referred to as *ab initio* molecular dynamics (AIMD) methods [37], although chemists tend to reserve the term for methods that solve the Schrödinger equation explicitly. The first method is the Born-Oppenheimer molecular dynamics (BO-MD), and it uses a similar scheme as the BO approximation in the electronic structure calculations: For each timestep, solve the electronic structure with stationary ions, then calculate the ionic movement with stationary electronic structure and recalculate the electronic structure with new ionic positions.

After solving the electronic structure, we can apply the Hellman-Feynman theorem and calculate the forces from the ground state energy as

$$\mathbf{F}_I = -\frac{\partial E\left[n_0\left(\mathbf{r}\right)\right]}{\partial \mathbf{R}_I}, \tag{33}$$

where the ground state density $n_0\left(\mathbf{r}\right)$, as well as the energy calculated from it are dependent on the ionic positions $\mathbf{R}_I$ through V_{ext}, as described in section 2.1.2. These forces yield ionic accelerations $\mathbf{a}_I = \mathbf{F}_I/m_I$, and together with the time step length, old positions and velocities a new set of ionic positions and velocities are calculated. There are various methods to calculate the values for the next step, as the discretization of time causes the ionic trajectory to drift away from the exact trajectory over time, particularly if they are calculated simply as $\mathbf{R}_{I,\text{ new}} = \mathbf{R}_{I,\text{ old}} + \dot{\mathbf{R}}_I \Delta t$ and $\dot{\mathbf{R}}_{I,\text{ new}} = \dot{\mathbf{R}}_{I,\text{ old}} + \mathbf{a}_I \Delta t$. One solution is a predictor-corrector method, where the next step is first calculated as such (predict step), and then the value is refined (correct step). In more sophisticated methods multiple prior values are taken into account [38]. The electronic structure of the next step can be calculated with the new ionic positions. The old electronic densities of few past steps are commonly used to calculate the initial guess for the self-consistent

loop. This helps in reaching the convergence, and in practice, a single BO-MD step in the middle of a simulation requires much less computational effort than the calculation of electronic density of the same ionic structure from scratch.

Another molecular dynamics method used in the present work is the Car-Parrinello molecular dynamics (CP-MD) [39]. It also uses the DF theory to calculate electronic structure, but after the initial electronic structure calculation the electronic KS-orbitals are coupled to the ionic movement and propagated along rather than kept stationary while the ions are moved, as was the case in BO-MD. In this scheme, the ground state of the electron orbitals is allowed a finite "thickness", in energy, where the electronic solution is allowed to vary and fictitious electron dynamics is used to couple electronic and ionic motion.

The formulation of CP-MD follows the Lagrangian mechanics with the added coupling to electronic wave functions. The Lagrangian is [40]

$$L = \mu \sum_i \int \left|\dot{\psi}_i\right|^2 \mathrm{d}\mathbf{r} + \frac{1}{2}\sum_I M_I \dot{\mathbf{R}}_I^2 - E\left[\{\psi_i\}, \{\mathbf{R}_i\}\right] + \sum_{i,j} \Lambda_{ij}\left(\int \psi_i^*(\mathbf{r})\,\psi_j(\mathbf{r})\,\mathrm{d}\mathbf{r} - \delta_{ij}\right), \tag{34}$$

where dot denotes a time derivative, ψ are the electronic orbitals, $\mathbf{R}_i$ and M_I the ionic positions and masses, Λ are Lagrange multipliers for the orthonormality constraint, and μ is the fictitious electron mass. Usually μ of the order of $10^2 m_e$-$10^3 m_e$ is used to make electron dynamics sufficiently slow to allow for a longer time step. However the time step required is still much shorter than what is required with BO-MD.

The equations of motion of this Lagrangian are then

$$\mu\ddot{\psi}_i(\mathbf{r},t) = -\frac{\delta E}{\delta \psi_i^*(\mathbf{r},t)} + \sum_j \Lambda_{ij}\psi_j(\mathbf{r},t) \tag{35}$$

$$M_I\ddot{\mathbf{R}}_I = \frac{\partial E}{\partial \mathrm{R}_I}. \tag{36}$$

This way the ground state does not need to be solved for every ionic configuration but rather the ground state can be propagated in time while moving the ions.

In the present work, BO-MD was used for the simulations of $Ge_{15}Te_{85}$ and $Ge_2Sb_2Te_5$, while the CP-MD was used with GaSb and $GaSb_7$.

3.3 Periodic boundary conditions

Imposing periodic boundary conditions (PBC) is a practical trick and an approximation, where one uses a small super cell for the material in question and multiplies that infinitely many times in one, two or three directions to model the bulk material. For crystalline structures with translational symmetry (this rules out so called quasicrystals), it is known that a wave function of an electron has the same translational symmetry [41] and it can be used with other symmetry operations as well [42]. In periodic crystals, the primitive cell can be used, and in some cases only a few atoms are needed to reproduce the crystalline structure; for

example the NaCl rock-salt structure has two atoms in its primitive cell while the GaSb zinc blende structure has eight. This makes it possible to model a bulk crystal with very little computation. In nature, however, crystalline materials have never perfect periodicity over a macroscopic length scales but it is a reasonable approximation in most cases.

Using primitive cell neglects random defects, and their inclusion requires an increased super cell sizes to allow sufficient statistics and randomness in the defect placement. For disordered solids, a larger super cell sizes have obvious advantages as the materials are assumed to have no periodicity in the first place. The larger system sizes improve statistics and reduce the artificial effects of the imposed periodicity, and this leads to more accurate structural models. A general rule of thumb with disordered materials is that structural features up to a distance of one half of the super cell size can be regarded as reliably modeled. With large super cell it is sufficient to calculate the electronic structure in only one k-point (Γ) in the Brillouin zone, but for smaller structures it is necessary to have multiple (up to a few tens of) k-points to properly sample the band structure.

3.4 Temperature control

A Nosé-Hoover thermostat is a common way to implement temperature control in molecular dynamics simulations. It introduces an additional coupling in the system with a thermostat, which drives the system towards a target temperature (ionic thermostat) or target electronic kinetic energy (electronic thermostat) [43, 44]. The coupling is done by introducing an extra degree of freedom s into the Hamiltonian of the system. The extended Hamiltonian is then expressed in a new set of (virtual) variables $\mathbf{r}_i$, $\mathbf{p}_i$ and t. The real variables (primes) can be expressed in terms of the virtual variables as $\mathbf{r}'_i = \mathbf{r}_i$, $\mathbf{p}'_i = \mathbf{p}_i/s$ and $t' = \int^t s^{-1}\mathrm{d}t$. The new Hamiltonian is then

$$H = \sum_i \frac{\mathbf{p}_i^2}{2m_i s^2} + V(\mathbf{r}) + \frac{p_s^2}{2Q} + gTk\ln s, \tag{37}$$

where p_s is the conjugate momentum of s, Q is the mass of the virtual degree of freedom, T is the target temperature of the thermostat, k is the Boltzmann constant and g is essentially the number of degrees of freedom in the system.

This Hamiltonian results in a set of equations of motion, which are dependent on s. The dependence can be eliminated [44] and the simplier equations of motion can be written as

$$\dot{\mathbf{r}}_i = \frac{\mathbf{p}_i}{m_i} \tag{38}$$

$$\dot{\mathbf{p}}_i = F(\mathbf{r}_i) - \zeta\mathbf{p}_i \tag{39}$$

$$\dot{\zeta} = \left(\sum_i \frac{\mathbf{p}_i^2}{m_i} - gkT\right)\cdot\frac{1}{Q} \tag{40}$$

Comparing the two first equations with the coordinate equation of motion without a thermostat [Eq. (36)] shows that the thermostat controls temperature essentially by scaling the acceleration of ions with a term proportional to the velocity of the ions (temperature). The coefficient of velocity is the thermodynamic friction coefficient $\zeta \equiv p_s/Q$, and it follows the third equation listed above.

Multiple thermostats can be chained to achieve a damping effect on the thermostat behavior. When using chained thermostats, the first thermostat directly changes the ionic or electronic kinetic energy and the second thermostat affects the amount of change. The subsequent thermostats work similarly, each affecting the previous one and being affected by the next one. The last thermostat can be either uncontrolled, meaning that it doesn't have a subsequent thermostat that would control it, or can be coupled back to the second-last thermostat in a loopback fashion.

3.5 Reverse Monte-Carlo

Reverse Monte Carlo (RMC) is a mathematical method to fit a distribution of atomic structures into a set of experimental data and other constraints. Coordination numbers, bond angles and other structural parameters are used as the user-specified constraints. RMC++ [45] was the code used in present work. In contrast to Monte-Carlo scheme, where one uses (pseudo)random procedure to calculate a probability distribution for a given phenomena, the RMC scheme uses experimental probability distributions (pair distribution functions, structure factors, etc.) as the input, hence the name "reverse" Monte-Carlo. In RMC method, the experimental data and user constraints form an acceptance criterion

$$\chi^2 = \frac{1}{\delta^2} \sum_k \left(S_k^{\text{comp}}(Q_k) - S_k^{\text{expt}}(Q_k) \right)^2, \tag{41}$$

where the sum is over data points k and superscripts denote computed and experimental $S(Q)$.

The computer then randomly displaces an atom in the candidate structure and recalculates χ^2, if $\chi^2_{\text{new}} < \chi^2_{\text{old}}$ the move is always accepted and if $\chi^2_{\text{new}} > \chi^2_{\text{old}}$ then the move is accepted with a probability $\exp\left[-\left(\chi^2_{\text{new}} - \chi^2_{\text{old}}\right)/2\right]$. This way the structure is gradually changed to another one with a better fit with the acceptance criterion. In practice, RMC will return *a distribution of structures* that statistically match the input data. The user constraints are important in addition to the experimental data because the RMC method is a purely mathematical method and will prefer the most disordered atomic configurations that fit the experimental data unless constrained [46]. RMC without correct constraints is known to produce flawed results, for example amorphous structures with metallic electronic density of states for $Ge_2Sb_2Te_5$ [47].

4 Materials

This thesis considers phase-change (PC) materials, which is an important family of chalcogenide alloys. PC materials are used in optical storage, i.e. rewritable CD, DVD, and Blu-ray Disc. Recently, they have been utilized in electronic memory as well (phase-change random-access-memory, PC-RAM or PRAM). In this section, a short overview of the key concepts is laid out for the reader. There is a number of extensive review articles covering all aspects of phase-change memory, from theoretical foundations to manufacturing an array of memory devices. This section is mostly based on two of them, references [48] and[49].

As PC materials have two phases, crystalline and amorphous (disordered, glassy), I will start with an introduction to glassy materials. This is followed by the classical nucleation theory, which is a simplified model for crystallization. In this section I shall also describe modern computer memories, phase-change materials and phenomena, and have a closer look at the specific materials studied in this thesis.

4.1 Glasses

Most liquids form a glass if you cool them fast enough. The concept of a glass usually refers to an undercooled liquid-like structure where the atoms or molecules move much slower than in the liquid; the difference can be as high as 14 orders of magnitude. It is not clear why the material experiences such a change within relatively small (some fraction of melting temperature) change in temperature. The glass transition is not a phase-transition similar to thermodynamic transitions (e.g. melting, freezing) and the glass temperature T_g cannot be defined as one fixed number similarly to the transition temperatures of thermodynamic transitions [4].

Knowledge of glass physics can be useful in various fields, for example liquid physics or in "soft" condensed matter where glassy phases might occur in colloidal systems, emulsions, beer foam, proteins, or granular materials. The glass concept can also be applied to more exotic behaviors, for example in so-called "spin-glass" the magnetic disorder freezes in low temperatures similarly to the positional disorder in glasses [4].

Figure 2 is an Angell plot of various glasses adopted from ref. [50]. Glasses can be strong or fragile in a sense that relates to the stability of the local environment of an atom or a molecule over the glass transition, and this has nothing to do with the mechanical shattering of a piece of glass. Rather the strong glasses tend to have slow crystallization rates while the fragile ones crystallize faster. When vitrifying a material, the quench needs to be fast enough to achieve vitrification before crystallization happens, and thus fragile glasses are harder to vitrify. A textbook example of a strong glass is SiO_2, which has a local tetrahedral structure both, below and above the T_g [4], while fragile glasses generally do not preserve the local structure across T_g. The PC materials, such as $Ge_{15}Te_{85}$ and $Ge_2Sb_2Te_5$ can be classified as fragile glass formers [51, 52], and their viscosities change dramatically as a function of temperature at temperatures above T_g.

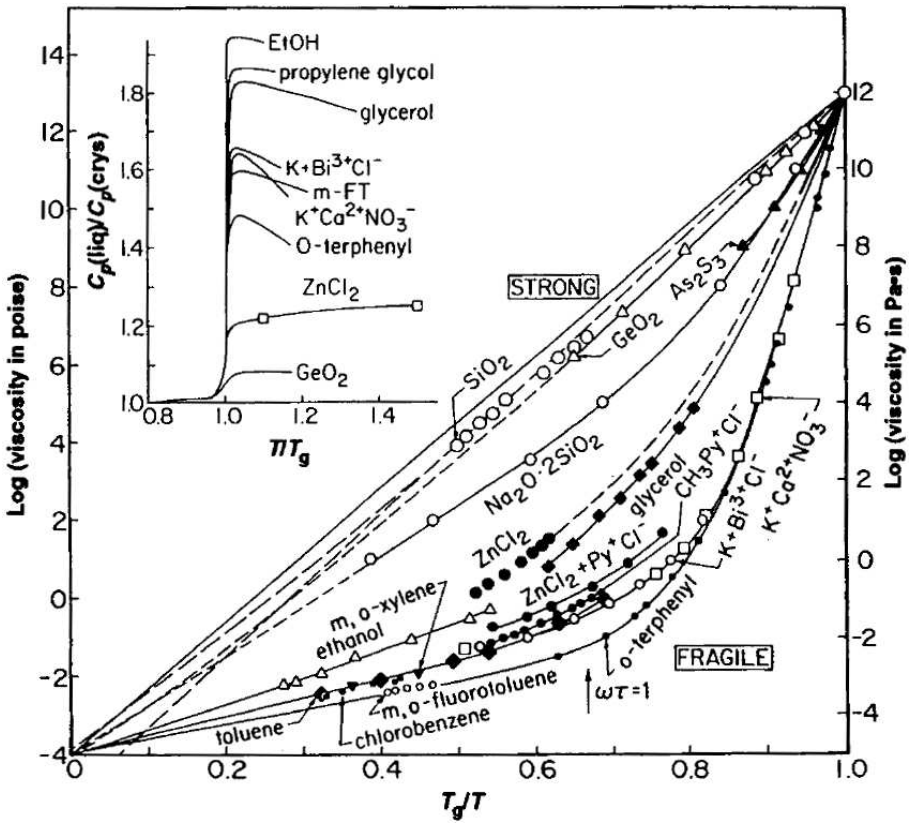

Figure 2: Angell plot of viscosity (log scale) as a function of T_g/T. "Strong" glasses follow the straight line, while "fragile" glasses have lower viscosities. Inset shows the jump in C_p at T_g, which generally increases with fragility. Adopted from ref. [50].

4.2 Classical nucleation theory

The classical nucleation (CN) theory is a theory that describes nucleation in liquids and amorphous materials. In the CN theory the formation energy of a nuclei with radius r is simply a sum of the free energy gained when a certain volume of the material is in crystalline phase and the free energy cost to form an interface between the crystalline and amorphous phases. The change in Gibbs free energy for a spherical crystallite with radius r is thus

$$\Delta G(r) = -\Delta G_\mathrm{ac}\frac{4}{3}\pi r^3 + \sigma_\mathrm{ac}4\pi r^2, \tag{42}$$

where ΔG_ac is the Gibbs energy difference between amorphous and crystalline phases per unit volume and σ_ac is the amorphous – crystalline interfacial energy per unit area [48]. For small r, $\Delta G(r)$ increases with radius, but after a critical nucleus size ($r_\mathrm{c} = 2\sigma_\mathrm{ac}/\Delta G_\mathrm{ac}$) it is energetically favorable for a nucleus to grow. The thermal fluctuations cause small nuclei to form and dissolve randomly, and after a while there is a nucleus with $r > r_\mathrm{c}$ which will continue growing.

Within the CN theory, one can model the heterogeneous nucleation with spherical cap model, where the crystal is assumed to grow spherically from an interface.

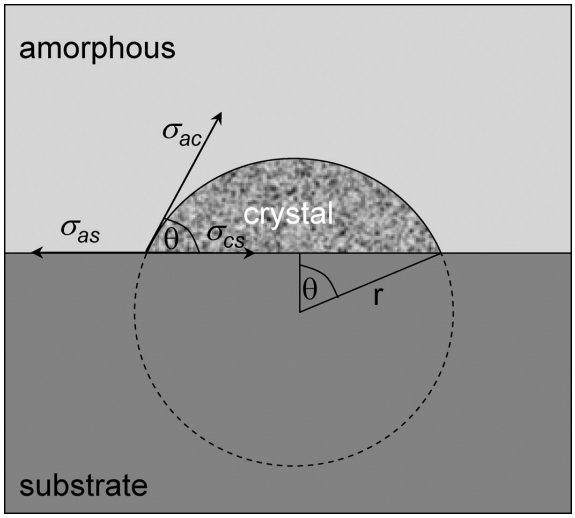

Figure 3: Spherical cap model for heterogeneous cluster formation. The crystal is assumed to have the shape of a spherical cap. θ is the wetting angle, and σ_{rmas}, σ_{rmac}, and σ_{rmcs} are the interfacial energies between the amorphous (a) and crystalline (c) phases and the substrate (s). Adopted from ref. [48].

The interface can be a substrate or an existing crystal volume. We can write the heterogeneous Gibbs free energy differences as

$$\Delta G^{\text{het}}(r) = -\Delta G_{\text{ac}} \frac{4}{3}\pi r^3 f(\theta) + \sigma_{\text{ac}} 4\pi r^2 \frac{1-\cos\theta}{2} - \pi (r\sin\theta)^2 \sigma_{\text{ac}}, \tag{43}$$

where

$$f(\theta) = \frac{(2+\cos\theta)(1-\cos\theta)^2}{4}. \tag{44}$$

The wetting angle (θ) is the angle between the existing interface and the newly grown spherical interface (fig. 3). We can compare the free energy for isolated nucleus and spherical cap of equal radii, for which the nucleation energy can be shown to be

$$\Delta G^{\text{het}} = f(\theta)\,\Delta G^{\text{hom}}. \tag{45}$$

In addition, the volume of spherical cap is the volume of a sphere multiplied by $f(\theta)$, which means that the energy required per unit of crystalline volume – or number of atoms for that matter – is equal in both cases.

This leads one to think that it is not the low growth rate, which makes nucleation dominant PC materials to behave as they do but rather the exceptionally fast nucleation rate. On the other hand, nucleation rate and growth speed are temperature dependent [48] which enables one to tune the nucleation/growth ratio of a given material. In these situations, it is possible to switch the material from growth dominant to nucleation dominant, or vice versa.

4.3 Memory in modern computers

Computer memories can be divided in two categories according to the time they retain the stored data without operating power, *volatile* and *non-volatile* memory. Currently computers use both, and the development has lead to very distinct roles for both types: There is a very fast volatile memory to store frequently-changing data and much slower non-volatile memory to store persistent data. Modern DDR3 SDRAM memory has a latency time of ~10 ns, data rates of tens of gigabytes/s and a cost of few euros/GB, and is used for the working memory. On the other hand, long term storage is done with a hard disk drive which has a latency of milliseconds, data rate of hundreds of megabytes/s and a cost of few eurocents/GB. In comparison to SDRAM, hard disks have approximately 10^5 times longer latency, and 100 times slower data transfer, but are 100 times cheaper per byte. Solid state (flash) drives have become widely used during the last 5 years and are currently ~1 order of magnitude faster and more expensive than traditional hard disks with spinning plates.

DDR3 SDRAM memory consists of a large array of capacitors on an integrated circuit (IC) board which either have charge ("1" bit) or have no charge ("0" bit). However, the capacitors leak charge and will soon all show as "0" bit; this means that the memory needs to be read and rewritten (refreshed) before this happens. JEDEC standards define that the DDR3 SDRAM memory uses 7.8 μs refresh interval [53], corresponding to ~128 MHz refresh rate in order to preserve the stored data for as long as the computer is switched on. The order of magnitude of the time which DDR3 memory retains its data after power off is few microseconds. On the other hand, a hard disk drive can keep the data stored on magnetic plates for years after powered off. There have been ideas of a possibility to design a so-called universal memory that would have the speed of DRAM and also retain its data for long periods of time [54]. However, there is still much to be done until this kind of memory is in common use.

The most important characteristics of a candidate phase-change material for electronic memory are crystallization speed at room and at elevated temperature, melting temperature, resistances in both phases, endurance (cycling) and threshold switching parameters.

4.4 Phase-change materials

Technically, the term "chalcogenide" refers to compounds containing at least one element from the chalcogen group (group 16) of the periodic table. However, after the discovery of chalcogenide phase-change materials there have been found other materials which behave the same way but contain no elements from the group 16, for example GaSb. All phase-change materials studied in the present work contain either tellurium (group 16), antimony (group 15) or both, and this is true for most — if not all — materials that exhibit the rapid phase-change phenomena.

The existence of multiple distinguishable solid states for certain chalcogenide alloys has been known for decades. The early reports of the rapid and reversible switching between these states were reported in 1968 by S.R. Ovshinsky [55]. He described the materials as *oxide- and boron-based glasses and materials which contain the elements tellurium and/or arsenic combined with other elements such as those of*

groups III, IV and VI (groups 13, 14 and 16 in the modern IUPAC numbering) and used $Ar_{30}Ge_{10}Si_{12}Te_{48}$ for the measurements. This material is initially in a highly resistive state and can be switched to a conductive state by applying a voltage V_t across it (ranging from 2.5 V to 300 V, as a function of film thickness). If the voltage is removed, the material switches back to the resistive state. In the same paper, he also mentioned that some other compositions of the same elements have a *memory effect*, that is: the conductive state is preserved even if the voltage is removed. The resistive state can be restored with a large enough current pulse. This memory effect is in the center of the modern industrial use of chalcogenide phase-change materials.

The resistance change is not the only measurable difference between the different states. First report of an optically induced and measured phase-change in chalcogenide materials was in 1971 by Feinlieb *et al.* [56]. However, the early materials weren't suitable for industrial production. In 1987, Yamada *et al.* [57] reported a high-speed optical phase-change of $Ge_1Sb_2Te_4$ (GST-124) with cyclability up to 10^5 times. Such materials which could be switched and read with a laser became the first widely used phase-change memory materials in the form of rewritable disks (CD, DVD). The contemporary Blu-ray Discs are the latest addition to this family. Optical disks are mostly based on compounds on the pseudobinary GeTe-Sb_2Te_3 tie-line or on doping Sb_2Te with various elements [48].

The reversible switching is used to record data in small bits on the recording film that are either in resistive and non-reflective (amorphous) or conductive and reflective (crystalline) phase, and the different electric resistance or optical contrast is used to read the data. The memory effect means that the data stays in the memory for an extended period of time, making the memory operate as a *non-volatile memory*.

When considering a material for electronic phase-change memory, the key factors are cyclability, data retention and recrystallization speed. Phase-change memories commonly show cyclability of 10^8-10^{10} cycles, which is enough for most applications in storage class memories but not quite enough for a replacement of DRAM. A typical data retention requirement of a phase-change memory device is that the device must keep the written data for 10 years at 85°C with less than 1 failing device in 10^9. The amorphous to crystalline switch is always slower than the crystalline to amorphous switch, and thus the recrystallization speed places an upper bound for the switching speed of a phase-change memory. This directly affects the data write rate [49]. However, it is not trivial to find a material with fast crystallization speed and long data retention, which at first seem to be mutually exclusive. This is understandable as the required nonlinearity in the temperature dependence of crystallization speed is unusually large, and the usable PC materials are the ones where the crystallization speed is accelerated by a factor of $\sim 10^{17}$ when temperature is increased by a factor of ~2. When a PC material is deposited on a device, the as-deposited PC material is commonly amorphous, as the deposition process is carried out at below the crystallization temperature. This as-deposited (AD) phase can differ from the cycled melt-quenched (MQ) amorphous phase considerably [58], even though both are amorphous. However the behavior could also be approximately the same for both [59]. The awareness of this difference has helped to explain discrepancies between experiments and

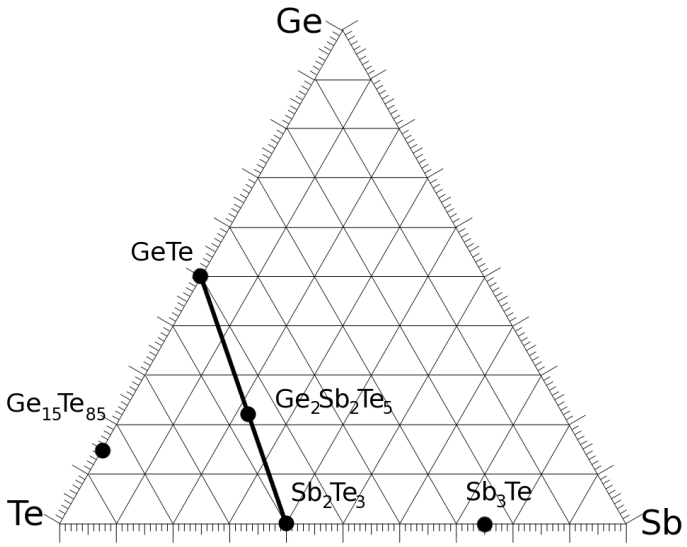

Figure 4: Ternary diagram of Ge-Sb-Te phase-change materials. The pseudobinary GeTe-Sb_2Te_3 line is drawn on the left and the Sb-rich PC materials reside on the right side near Sb_3Te. $Ge_{15}Te_{85}$ and $Ge_2Sb_2Te_5$ positions are marked. The plain ternary diagram base was adopted from Wikipedia (license: CreativeCommons Attribution-ShareAlike 3.0).

computer simulations of $Ge_2Sb_2Te_5$ [60].

The phase-change materials can be divided in two categories by their crystallization dynamics. The classification follows approximately the division between GeTe-Sb_2Te_3 pseudobinary alloys and the Sb-rich alloys. The former group is often referred to as the nucleation dominant PC material family and the latter as growth dominant. The ternary diagram for Ge-Sb-Te alloys (figure 4) shows this pseudobinary line and two of the materials studied in this thesis ($Ge_{15}Te_{85}$ and $Ge_2Sb_2Te_5$). The growth dominant Sb-rich materials, such as $Ag_{3.5}In_{3.8}Sb_{75}Te_{17.7}$ used in rewritable DVD disks, reside near the Sb-corner of the diagram with Sb_3Te. According to the CN theory, the nucleation dominated and growth dominated categories can be described as homogeneously nucleating and heterogeneously nucleating, respectively.

Threshold switching is a peculiar feature in PC materials. When an amorphous PC material is subjected to a large enough electric field, it can switch to a highly conductive *temporary* state within nanosecond timescale. If the voltage is left on, the current heats the material, crystallizing it and the material is switched. On the other hand, if the pulse is short enough the material does not experience a phase-change and will keep the high-resistance amorphous state after the field is turned off.

Threshold switching is visible in the I-V curve of a phase-change memory cell shown in figure 5, where the voltage across the cell is increased in the resistive amorphous state (full circles) until just below 1.2 V, where the voltage suddenly drops while the current increases. This negative differential resistance state is what causes the threshold switching. The current increases until a positive dif-

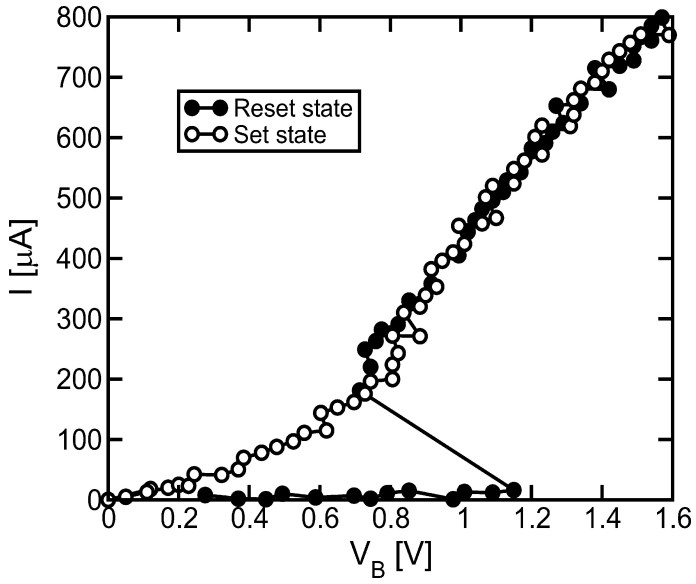

Figure 5: Measured I-V curves for a phase-change memory cell in the set (open symbols) or reset (filled symbols) states. The latter displays the threshold switching effect at about V_T = 1.2 V. Adopted from ref. [48].

ferential resistance state is reached; typically at this current the PC material is crystallized very rapidly, and the I-V curve follows closely that of the crystalline phase (open circles) [48]. Resistance switching is crucial for the operation of a phase-change memory cell, as it allows for two separate voltage regimes for reading and programming the cell and also reduces the required power for the switch operation, making the memory more power-efficient.

4.5 Phase-change materials studied in this thesis

In the following I shall describe the materials studied in this thesis as they are presented in the literature.

$\mathbf{Ge_{15}Te_{85}}$

The eutectic composition $Ge_{15}Te_{85}$ is a binary PC material and one of the first ones to show rapid switching [61]. The switching time has been measured to be as low as 5 ns [62]. It is regarded as a prototype PC material with a melting temperature of 648°C [63], and it has a very high crystallization temperature of 446-471°C, depending on the heating rate [64]. The crystalline structure is ambiguous, and there are studies that report signs of segregation. In the amorphous structure, germanium is predominantly tetrahedrally coordinated with edge- and corner-sharing $GeTe_4$ tetrahedra while tellurium prefers threefold coordination, and 26% of volume is occupied by nanosized cavities in computational structure model [65] evaluated by using a method as described in ref. [66]. Our aim was to extend the model presented in ref. [65] by using experimental measurements along with a larger simulation cell.

$Ge_2Sb_2Te_5$

$Ge_2Sb_2Te_5$ (GST-225) is one of the early PC materials utilized in optical storage. It is also one of the most studied. It was discovered in 1987 by a Yamada et al. [57]. It has a melting temperature of 620°C and a rather low crystallization temperature of 160°C [67]. Electric resistivity changes approximately 5 orders of magnitude upon phase change [67], while the difference in refractive index is of the order of 1.20 [68]. GST-225 shows segregation after repeated set-reset cycles, presumably due to the higher electronegativity of tellurium (5.49 eV) than that of antimony and germanium (4.6 and 4.85 eV, respectively), which causes tellurium to drift towards the positive electrode [49]. This effect can be minimized by cell design or alternating the direction of polarity.

It crystallizes in a metastable rock-salt structure, where, according to the most accepted model [48], tellurium atoms occupy one sublattice while the other contains randomly placed germanium and antimony atoms. 10% of the sites are vacant. However, distinction between antimony and tellurium atoms is hard and Nonaka *et al.* finds equally good match to experimental data by swapping all antimony in the lattice with tellurium [69]. There could also be order in the Ge/Sb sublattice [70].

$Ge_2Sb_2Te_5$ expands upon amorphization by ~7% and the volume of vacancies or voids increases slightly from 10% to 11.8%. The amorphous structure has small structural units that are reminiscent of the rock-salt structure, namely the so called ABAB-rings, and cubes and the amorphous structure contains traces of the crystalline order in the form of AB alternation. Ge and Sb atoms have mostly defective octahedral coordination in the amorphous phase with three short and three long bonds. In addition, one third of Ge are tetrahedrally bonded. The crystallization can then be viewed as a reorientation of these remnants of the ordered structure into a periodic crystal [66]. The rapid recrystallization in $Ge_2Sb_2Te_5$ is very important for the current and future PC memory applications. In this study we extended the understanding of the growth of a super critical nucleus in this material by using simulations in three different temperatures.

GaSb

GaSb is a stoichiometric compound that shows a high crystallization temperature of 275°C [67] and fast crystallization speed of 19 ns [71]. The former makes GaSb a potential material for memory cells used at higher temperatures, for example in automobiles. The GaSb melting temperature is 705°C [72]. The crystalline structure is a cubic "zinc blende" structure where the elements are completely mixed in tetrahedral sites, and ideally the structure contains no homopolar bonds. Crystallization characteristics shows nucleation-dominancy in a static laser-tester study [73]. Not much is known about the structures of amorphous Ga/Sb films. In this study our goal was to create models for the AD and MQ polymorphs of GaSb, and to study their differences and similarities.

$GaSb_7$

$GaSb_7$ is a PC material, which crystallizes in a growth-dominated fashion typical for an Sb-rich material [74]. The composition is very close to the eutectic $Ga_{12}Sb_{88}$. The melting temperature of $GaSb_7$ is 590°C [72]. Crystallization temperature varies between 233°C (as-dep.) and 210°C (after write-erase cycle) [74]. The crystallization temperature is ambiguous because there are signs of segregation to elemental Sb and GaSb regions: With segregation, Sb regions can crystallize at ~187°C and GaSb regions closer to 350°C [73], making the material semi-crystalline over a wide temperature range. The segregation can explain also the discrepancy between crystallization times as high as 750-1000 ns and as low as 5 ns for as-deposited (longest times) and melt-quenched (shortest times) amorphous samples [71, 73]. In this study our goal was to create models for the AD and MQ polymorphs of $GaSb_7$, and to gain information on why the recrystallization speed of this material differs between the AD and MQ polymorphs [71], while in the GaSb it does not.

5 Results and discussion

5.1 Computational details

All simulations were performed with the CPMD code [36], periodic boundary conditions, single point (**k**= 0) in the Brillouin zone, and in NVT ensemble (constant number of particles N, volume V, and temperature T). Temperature was controlled with a Nosé-Hoover thermostat (chain length 4, frequency 800 cm^{-1}) [43]. Scalar-relativistic Troullier-Martins pseudopotentials [34] were used with a kinetic energy cutoff of 20 Ry for the plane-wave basis. In addition to these, the following parameters were used in the respective simulations: TPSS functional [27] in the geometry optimizations of $Ge_{15}Te_{85}$ and PBEsol [23] for all other simulations. BO-MD with a timestep of 3.0236 fs (125 a.u.) for molecular dynamics of $Ge_{15}Te_{85}$ and $Ge_2Sb_2Te_5$ and CP-MD [39] with a timestep of 0.1693 fs (7 a.u.) and fictitious electron mass of 1200 m_e for the molecular dynamics of GaSb and $GaSb_7$.

TPSS was used to optimize the $Ge_{15}Te_{85}$ because it has been shown to reproduce the various parameters of crystalline tellurium well (lattice parameters, bond lengths and angles, and the cohesive energy), in particular it is better than PBEsol [75, 76]. However, due to the increased computational cost, it was impossible to use it throughout all simulations, and we decided to use PBEsol for the MD part. The reason for using CP-MD was that we were unable to get the BO-MD calculations for Ga-containing structures to work properly. We do not have a clear reason for this, but it may be related to the peculiar properties of gallium, e.g. metallicity, low melting temperature and unique crystal structure consisting of Ga_2 dimers. Otherwise, BO-MD was used as it can be tuned to perform much faster, similarly to the reasoning for using PBEsol.

5.2 Structure of $Ge_{15}Te_{85}$

5.2.1 Model structures and experimental fitting

We studied the amorphous structure of the prototypical $Ge_{15}Te_{85}$ PC material by BO-MD simulation and a subsequent RMC refinement. Both methods were important: If one would use only the simulation method the model structure would have a slightly better energy (calculated with the DF theory), but the pair distribution functions and total structure factors would be worse. Similarly, when using only RMC the result would agree better with the experimental data but have much worse DF energy.

The structure was based on a 216-atom melt-quenched amorphous structure from an earlier study [65]. The super cell of the 216-atom structure was a cube with 19.7 Å sides, and the structure was repeated periodically as it would be in a simulation. From the repeated structure, a larger super cell with a side of 27.08 Å was cut out, and the atoms near the new super cell edges were adjusted not to interfere with periodicity. A self-made code was written for this, which worked as a steepest descent geometry optimization with a hard-sphere potential for atoms near the edges. This resulted in a 560-atom structure with experimental number density (0.0282 $Å^{-3}$) and exact 15:85 composition.

Simulated annealing was performed on the structure to remove any artifacts that would otherwise result from the enlargement of the super cell in the above-mentioned manner. The structure was heated to 500 K, which is below the melting point of $Ge_{15}Te_{85}$ (680 K) and annealed in five steps of 20 ps each at 500, 450, 400, 350 and 300 K. After the annealing the structure was optimized. The optimized structure is referred to as "DF-opt" structure in the rest of this section and was used as one base structure for RMC-refinement. This structure should be representative of the set of structures in the MD simulation trajectory; for this reason we used the MD trajectory data for better statistics when possible. All BO-MD runs were done using the PBEsol functional, whereas the geometry optimizations were done with the TPSS functional, both of which are discussed in sec. 2.2.1.

An alternative base structure, referred to as "ideal" structure was also created. This structure was created with a hard-sphere run using the RMC++ code and a subsequent long RMC run to fit the structure to the experimental data as well as possible. This structure was also optimized using the TPSS functional and the DF energy was 10.15 meV/at. above the DF-opt structure energy.

The base structures were then fitted to experimental neutron diffraction (ND) and x-ray diffraction (XRD) data. Various different sets of constraints for RMC were tested to achieve as good fit to the experimental data with energy as close to the DF minimum energy as possible. When starting from an optimized structure, the RMC improves the fit to experimental data at the cost of increasing structure energy, and an energy of 100 meV/at. above the DF-opt structure energy was decided as the target for refined structure energy. Particularly, the ND total structure factor was hard to reproduce with a low energy structure. The set (a) was the best one that was based on the DF-opt structure and disallowed Ge-Ge bonds, set (b) was the best one that was based on the ideal structure and disallowed Ge-Ge bonds, and set (c) was the best one that allowed Ge-Ge bonds. The first two were consistent with earlier models that did not allow Ge-Ge bonds (for example [46, 77, 78]) while the last one was different. When fitting structure (c) to the experimental data, it was noted that changing the weights of ND and XRD data sets (adding more weight to ND) resulted in good fit for the ND data with little or no change in the XRD fit. However, in the other two [(a) and (b)] changing the weights did not improve the overall fitting quality.

The minimum inter-atomic distances in the RMC refinement were Ge-Te: 2.55Å, Te-Te: 2.70 Å, and Ge-Te 3.50 Å (Ge-Ge bonds forbidden) or 2.50 Å (Ge-Ge bonds allowed). The RMC refinement runs targeted to 100 meV/at. energy were short, only 10 000-15 000 accepted moves were needed to raise the energy by that amount. The maximum displacement of an atom was 0.05 Å.

The results are listed in table 1 and the comparison with experimental $S(Q)$ graphs is in figure 6. We used an iterative RMC refinement scheme, where a base structure was first refined with RMC (iteration #1), then re-optimized with the DF theory, refined again (iteration #2), and so on in order to see whether subsequent geometry optimization-RMC refinement cycles would drive the structure into a new energy minimum in the configuration space. This was not the case, and the resulting structures were similar for all iterations. This indicates that each re-optimization returned the structure close to the original base structure, and the next refinement produced again a structure similar to the previous refined

Table 1: ND and XRD values of $\langle \chi^2 \rangle$ ($\delta = 0.01$, average over data points) and total energies during iterative refinement. Energies are in meV/atom with respect to the DF energy minimum.

	structure (a)			structure (b)			structure (c)		
iter.	$\langle \chi^2 \rangle_{\mathrm{ND}}$	$\langle \chi^2 \rangle_{\mathrm{XRD}}$	ΔE	$\langle \chi^2 \rangle_{\mathrm{ND}}$	$\langle \chi^2 \rangle_{\mathrm{XRD}}$	ΔE	$\langle \chi^2 \rangle_{\mathrm{ND}}$	$\langle \chi^2 \rangle_{\mathrm{XRD}}$	ΔE
1	2.76	2.06	101	2.64	2.11	105	2.10	2.03	103
2	2.69	2.09	97	2.57	2.11	106	2.02	2.12	100
3	2.84	1.87	100	2.86	2.06	102	2.03	2.04	102
4	2.88	2.04	95	2.58	2.11	102	2.02	2.01	104
5	2.76	1.88	98	2.63	2.11	102	2.10	1.97	101

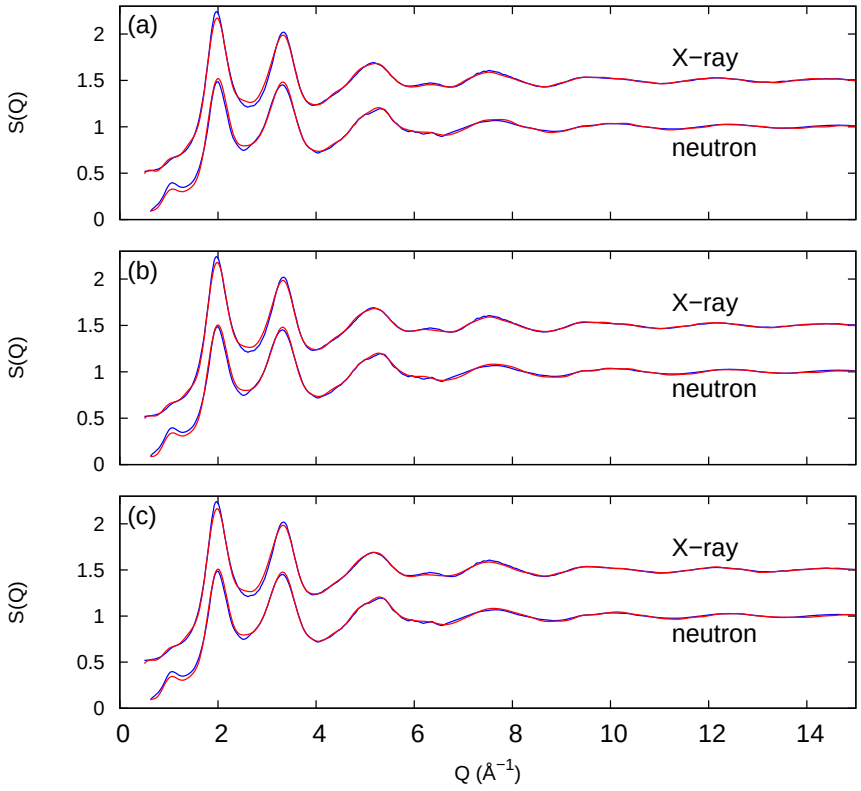

Figure 6: $S(Q)$ fits for samples of (a), (b), and (c) structures. Red: calculation, blue: experimental. The x-ray $S(Q)$ has been shifted by 0.5 units.

structure.

The results of the RMC refinement (table 1) show that all three structures fitted the XRD structure factor well, with the structure (b) slightly (by ~0.1 units) behind the other two. The ND structure factor was different with structures (a) and (b) fitting it ~0.5 units worse than structure (c) with (b) ~0.1 units better than (a). This indicates that Ge-Ge bonds in model structures, albeit in small numbers, improve the structure in terms of the DF energy and the agreement with both the ND and

Table 2: Distances and coordination numbers in *a*-$Ge_{15}Te_{85}$. r^{max}_{X-Y} (r^{min}_{X-Y}): first PDF maximum (minimum), N_r: total (structural) coordination number, and n_{X-Y} partial coordination number. N_c: chemical coordination numbers. N_r and n_{X-Y} were determined with bond cutoff of 3.0−3.3 Å. In the MD and DF opt column, the chemical coordination numbers are calculated from the DF-opt structure while the rest is averaged over the 300K MD trajectory.

Structure	(a)	(b)	(c)	MD and DF opt
$r^{\max}_{\text{Ge–Te}}$ (Å)	2.58	2.58	2.58	2.65
$r^{\max}_{\text{Te–Te}}$ (Å)	2.74	2.73	2.74	2.84
$r^{\min}_{\text{Ge–Te}}$ (Å)	3.12	3.12	3.10	3.07
$r^{\min}_{\text{Te–Te}}$ (Å)	3.12	3.12	3.15	3.15
N_r(Ge)	3.63±0.13	3.60±0.10	3.71±0.13	3.72±0.28
N_r(Te)	2.21±0.14	2.22±0.16	2.21±0.13	2.32±0.34
$n_{\text{Ge–Te}}$	3.63±0.13	3.60±0.10	3.58±0.12	3.62±0.27
$n_{\text{Te–Ge}}$	0.64±0.02	0.64±0.02	0.63±0.02	0.64±0.05
$n_{\text{Ge–Ge}}$	0	0	0.13±0.01	0.11±0.01
$n_{\text{Te–Te}}$	1.57±0.12	1.58±0.13	1.58±0.11	1.69±0.30
N_c(Ge)	3.44	3.50	3.55	3.53
N_c(Te)	2.06	2.04	2.05	2.13
$n^{\text{chem}}_{\text{Ge–Te}}$	3.44	3.50	3.45	3.43
$n^{\text{chem}}_{\text{Te–Ge}}$	0.60	0.61	0.59	0.60
$n^{\text{chem}}_{\text{Ge–Ge}}$	0	0	0.10	0.10
$n^{\text{chem}}_{\text{Te–Te}}$	1.46	1.43	1.46	1.53

XRD experimental structure factors.

The electronic structure shows semiconductor characteristic with a very small band gap. The gaps were of the order of 0.1 eV, and there were several impurity states nearby. This is typical for DF calculations of PC materials, which have small (semiconducting) band gaps, and the standard DF theory further underestimates band gaps for solids. Usually, RMC refined structures tend to have metallic electronic structure, but a semiconductor-like behavior can be achieved with bond angle constraints, as is the case here.

5.2.2 Bonds and coordination numbers

Table 2 shows the radii of first maxima ($r^{\max}$) and first minima ($r^{\min}$) of the Ge-Te and Te-Te partial pair distribution functions (PDF, $g(r)$), and coordination number values for the structures. The RMC refinement caused the first peak of the PDF to move to the minimum allowed distance of the two atoms and narrow down, and thus the $r^{\max}$ and $r^{\min}$ values of the three RMC refined structures are very similar differing by only 0.03 Å at most. The partial PDF peaks calculated from the MD trajectory are both at slightly higher radii than the peaks in RMC structures (by 0.07-0.10 Å) due to the choice of using the shortest inter-atomic distance of MD structure as the minimum inter-atomic distance in the RMC refinement.

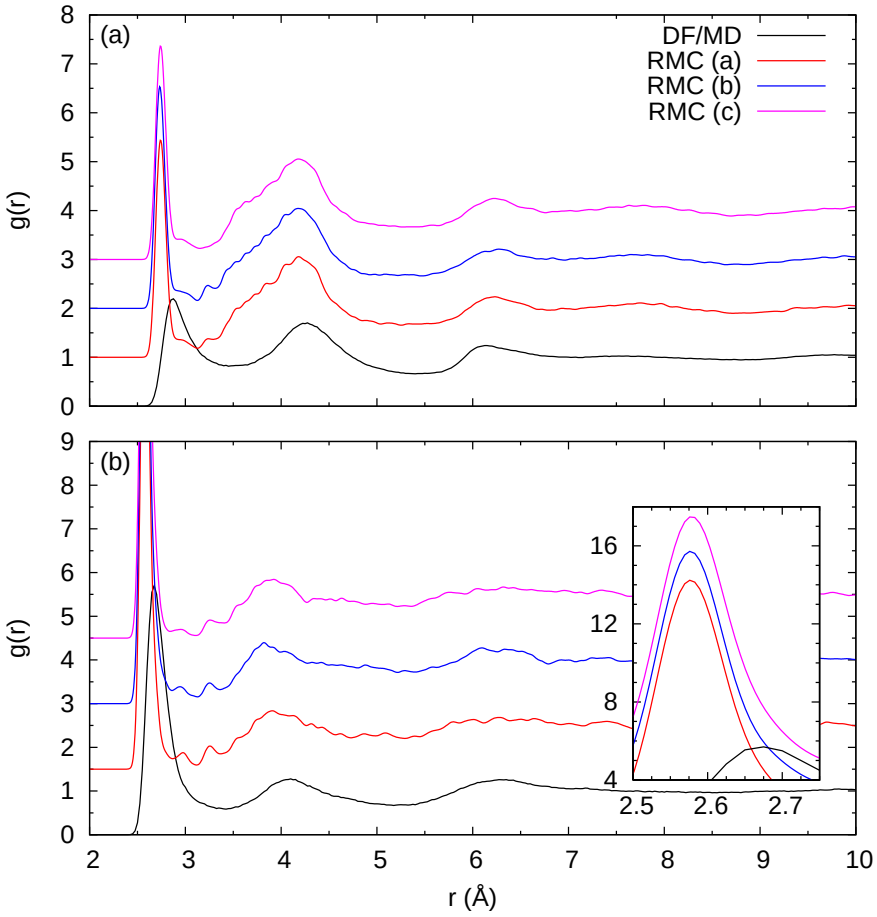

Figure 7: Te-Te Partial PDF (a) and Ge-Te partial PDF (b) for the RMC structures (a)-(c) and MD simulation at 300 K (annealing, PBEsol functional).

Together with the peak sharpening, this led to the result where the first peak of every structure starts at the same distance, but as the MD peak is wider, the maxima are at longer distances in comparison to the RMC structures. It is also worth noting that the EXAFS values for Ge-Te (2.60±0.02 Å) and Te-Te (2.79±0.02 Å) are between the $r^{\max}$ values of RMC structures and MD, being slightly closer to the RMC values. The difference between the RMC structures and MD is also visible in figure 7, where the peaks of structures (a), (b) and (c) are practically on top of each other, while MD peak starts at same distance but is wider and not as high.

The partial coordination numbers are similar for Ge-Te and Te-Ge atom pairs. Ge-Ge coordination number is of course different for structures where Ge-Ge bonding is not allowed [structures (a) and (b)] and where it is allowed (structures (c) and DF-opt) but the Ge-Te coordination does not change when disallowing Ge-Ge bonds, which leads to Ge total coordination being lower in structures (a) and (b). Te-Te coordination is ~0.1 lower in all three RMC structures than in DF-opt structure.

In addition to the atomic structure, it is possible to study chemical bonding by projecting the Kohn-Sham eigenfunctions on the atomic orbitals. In this scheme,

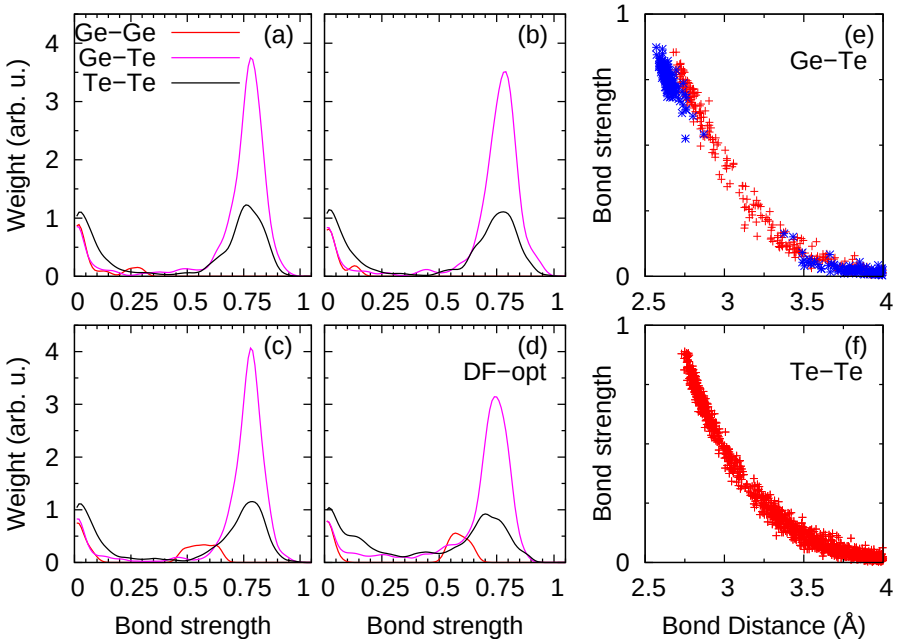

Figure 8: Chemical bond orders (strengths) in (a), (b) and (c) structures, and DF-opt (d). The chemical bond strength is plotted against bond length for Ge-Te (e) and Te-Te (f) bonds in DF-opt. For (e), red denotes threefold coordinated Ge, and blue fourfold coordinated Ge.

a single covalent bond would have a bond strength of one. This shows how strongly two atoms are bonded according to DF theory and doesn't necessarily follow the inter-atomic distance directly.

Figure 8 shows the bond order plots (left and middle columns) for the RMC and the DF-opt structures. The Ge-Ge bonds are visible in bottom panels, and they are generally weaker than the other bonds. Ge-Te and Te-Te bonds are mostly between 0.6 and 0.9 bond strength, while Ge-Ge bonds are between 0.5 and 0.65. The second nearest-neighbors are visible near zero strength, and there is less weight between the nearest and the second nearest-neighbor peaks in the RMC structures when compared to the DF-opt structure, which is consistent with the sharpened first maxima in PDF (see figure 7).

The bond strengths can be used to calculate coordination numbers, and the chemical coordination numbers N_c are shown in table 2. We used a bond strength cutoff of 0.4 based on the bond strength plots in figure 8[(a)-(d)], and 0.4 is approximately the value where the weight from nearest-neighbor bonds vanishes. Chemical coordination numbers are slightly below N_r, which are calculated with the cutoff radius. N_c are within the error bounds of N_r in the DF-opt structure and near the bounds of the RMC refined structures. The N_c of RMC refined structures is consistently just below the error bound, which indicates that the RMC refinement causes some atom pairs to be within a bonding distance of each other, but they do not have electronic bonding according to the DF theory. We also evaluated the distances where $N_r = N_c$, and the corresponding values (for DF-opt) are Ge-Te: 3.03 Å; Te-Ge: 3.01 Å; Ge-Ge: 3.16 Å; and Te-Te: 3.06 Å. These values correspond to the average coordination with minimum bond strength of

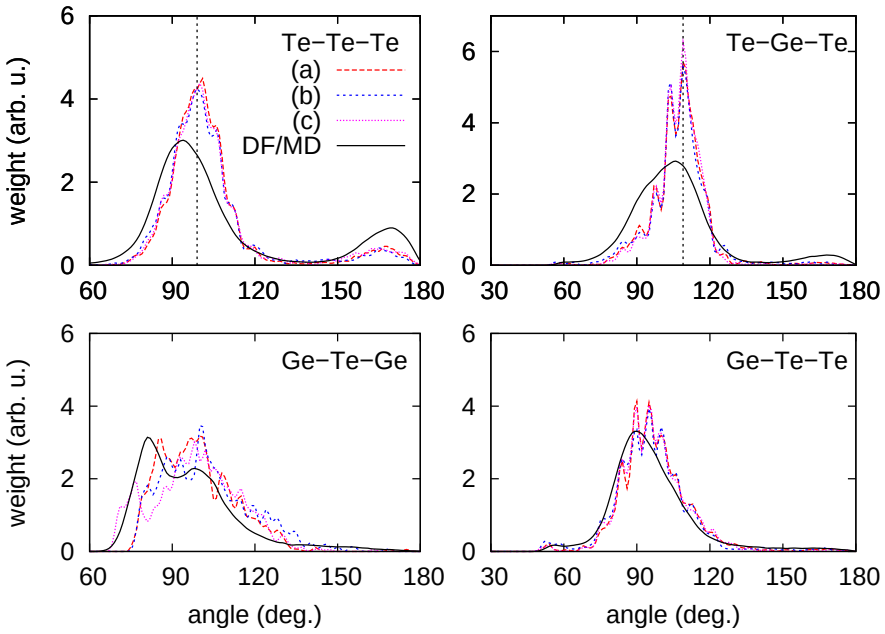

Figure 9: Bond angle distribution of the RMC-structures and MD trajectory. Red: structure (a), blue: structure (b), magenta: structure (c), black: DF/MD. Vertical dashed lines denote 99° in Te-Te-Te and 109° in Te-Ge-Te, the preferred angles during RMC refinement.

0.4 in a structure which is optimized with DF theory and serve as an estimate for reasonable radial cutoff distances.

The bond angle distributions with a bond cutoff distance of 3.2 Å are shown in figure 9. In general, the bond angles are close to octahedral. The Te-Ge-Te and Ge-Te-Ge plots show a shoulder and a dual maxima, respectively, which are signs of two distinct local environments for germanium. The existence of octahedral and tetrahedral local environments for germanium is shown also in figure 8(e), which display the bond distance and bond strength plotted for threefold and fourfold coordinated (as per chemical coordination) germanium atoms in red and blue, respectively. The threefold coordinated germanium have longer shortest bonds, and there is no distinct gap between first and second coordination shells. This is consistent with a distorted octahedral local environment, while the fourfold coordinated Ge is consistent with a tetrahedral local environment with shorter bonds, higher bond strengths, and a distinct gap between the first and second coordination shells. Figure 10 shows the distance distributions of nine nearest-neighbors of Ge atoms, similarly to the analysis performed by Raty *et al.* [79]. Signs of the two environments are yet again visible in figure, where the second to fourth nearest-neighbor plots have dual maxima and fifth and sixth neighbor plots have long shoulder or tail towards shorter distances. Approximately half of the germanium atoms belong to each of these environment types, as shown in table 3 with structure (c) having the most fourfold coordinated germanium (56%) and (a) the least (45%). Tellurium atoms are mostly twofold coordinated with a smaller fraction (~10-15%) of threefold coordination.

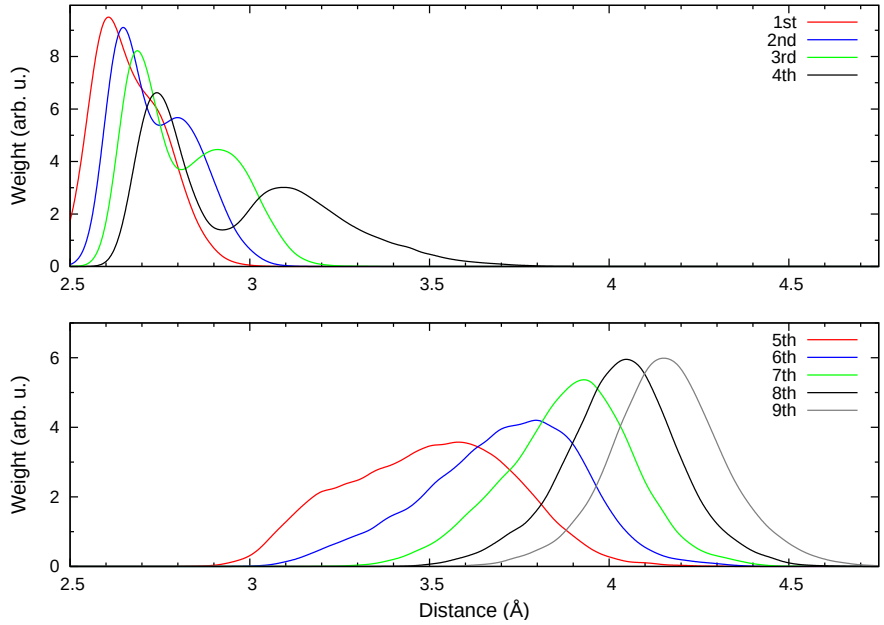

Figure 10: Nearest-neighbor distance distributions in DF/MD around Ge atoms.

Table 3: Nearest-neighbor analysis of Ge and Te (atomic %) using a chemical bond strength cutoff of 0.4 for neighbor search (see Figure 8.)

Atom	Neighbors	(a)	(b)	(c)	DF-opt
Ge	$GeTe_3$			7	7
	Te_4	45	52	49	45
	Te_3	54	45	41	45
Te	$GeTe_2$	5	6	4	7
	Te_3	3	3	4	7
	Ge_2	7	7	7	7
	GeTe	31	31	30	28
	Te_2	47	45	46	44

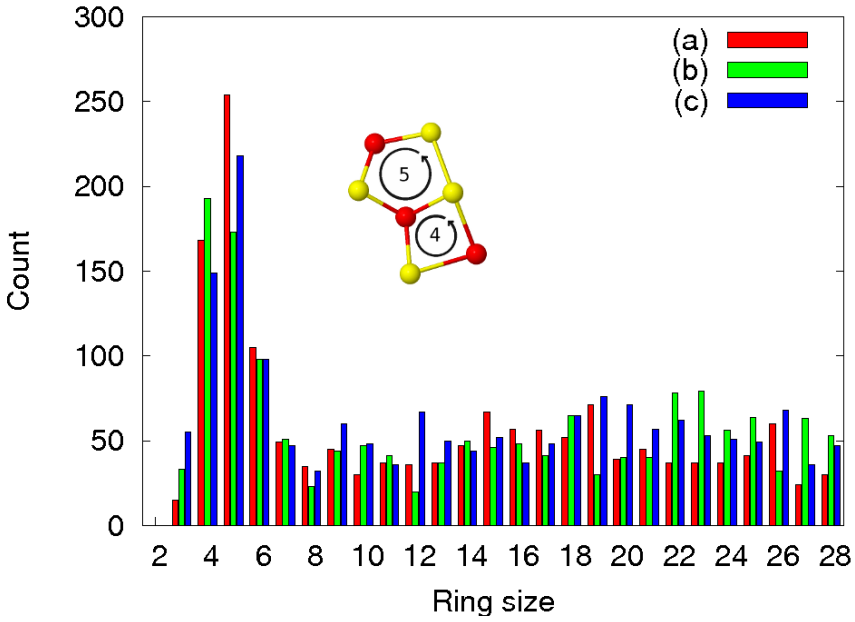

Figure 11: Ring size statistics of structures (a)-(c)

5.2.3 Medium range order

The medium range order is a term used to describe atomic order or arrangements at length scales just beyond the first and second nearest-neighbor distances. $Ge_{15}Te_{85}$ has a so-called first sharp diffraction peak (FSDP) in the total structure factor (see fig. 6, at small Q). The FSDP is predominantly visible in the ND total structure factor, and not in XRD, which indicates that it is related to germanium atoms rather than tellurium. This is because tellurium is a stronger x-ray scatterer than germanium (atomic numbers 52 and 32, respectively) but for ND the case is quite the opposite (bound coherent scattering lengths are 5.68 and 8.19 fm, respectively [80, 81]). The peak is at a Q range between 1.0 and 1.1 Å^{-1}, which corresponds to a length scale of $2\pi/Q \simeq 6.0 \pm 0.3$ Å.

The medium range order is affected by cavities, which are abundant in this material, and the existence of large irreducible rings, which surround the cavities and thus be quite large. Cavities were studied by placing a dense grid on the structure and checking for each grid point if the point was farther than 2.8 Å from all atoms, and then constructing the cavities with Voronoi prescription between these points and the nearby atoms, as described in ref. [66]. The cavities calculated this way comprise 22-24% of the volume in the RMC refined structures and 21.5% of the volume in the DF-opt structure. As mentioned before, the large volume of cavities and also their irregular shapes facilitate the formation of large rings around them. Figure 11 shows that smaller rings (4-6 atoms) are the most common, but the existence of large rings even up to (and beyond) 20 atoms is possible only due to cavities that entangled rings can surround without being shortcut in the middle.

A special class of rings can be separated, namely the so-called ABAB-rings where germanium and tellurium atoms alternate. The fraction of germanium

Table 4: Distribution of types of Te (I-III) and percentage of Ge in four-membered *ABAB* rings. Te(I) is directly bonded to germanium, Te(II) is not directly bonded to germanium but bonded to Te(I), and Te(III) are all others.

	(a)	(b)	(c)	DF-opt
Te(I)	48	49	47	47
Te(II)	26	26	25	27
Te(III)	26	25	27	26
Ge (*ABAB*)	15	14	20	27

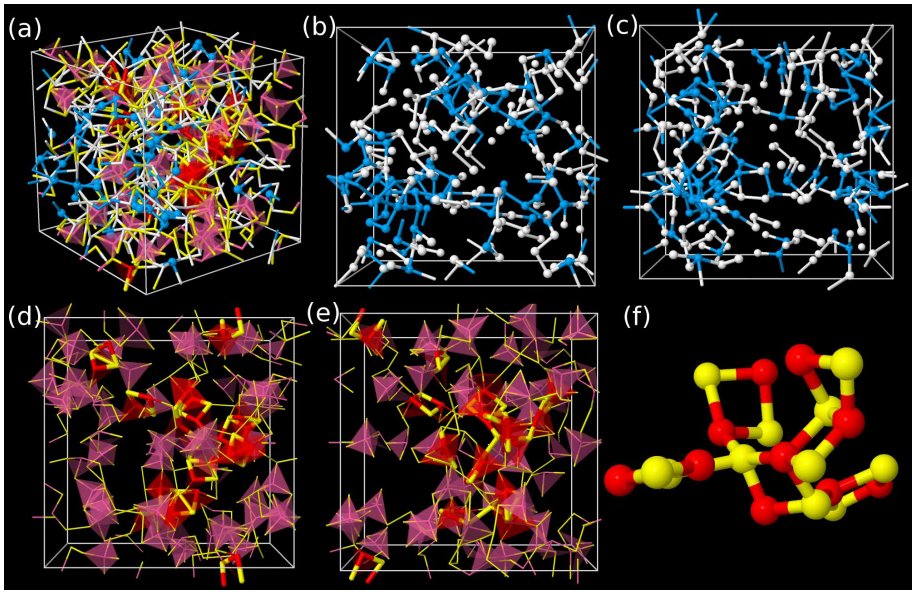

Figure 12: DF-opt sample: (a) Overview, (b-c) Te atoms not bonded to Ge [Te(I) and Te(II)] from front and right, (d-e) Ge and bonded Te atoms [Te(I)] from front and right, and (f) the largest cluster of *ABAB* rings. Red (thick): Ge atoms in *ABAB* rings, magenta: other Ge, yellow: Te(I), white: Te(II), blue: Te(III). Te(I)-Te(III) are defined in Table 4.

atoms in fourfold ABAB rings is listed in table 4, and the fraction of tellurium atoms is always $15/85 \simeq 0.18$ times that of germanium because of the alloy composition, while the number of atoms in the rings is equal. ABAB-rings are found to be relevant in $Ge_{50}Te_{50}$ and $Ge_2Sb_2Te_5$ [66], but they also seem to exist in $Ge_{15}Te_{85}$. The four-membered ABAB-rings (squares) can form clusters, which are the building blocks of crystalline $Ge_{50}Te_{50}$, and a 21-atom cluster of ABAB squares was found in the DF-opt structure. An overview of the DF-opt structure is shown in figure 12(a) and the panel (f) shows the cluster.

Tellurium atoms can be divided into categories, where Te(I) atoms are bonded to germanium, Te(II) atoms are bonded to Te(I) atoms but not to germanium, and Te(III) atoms are the rest [no connection to Ge or Te(I)]. The fractions are shown in table 4. It turns out that approximately half of tellurium atoms belong to the Te(I) group, which means that the other half of tellurium atoms are not bonded to germanium. These tellurium may – in principle – segregate, but there is no such sign: Instead of forming larger Ge-free volumes, they form a thin mesh [see fig. 12(b)-(c)] where the Ge-Te bits [see fig. 12(d)-(e)] are spatially quite uniformly distributed. There is slightly more GeTe in the right half of the panels (d) and (e), which indicate that there is locally more GeTe bits in that part of the super cell.

5.2.4 Conclusions

The amorphous model structures for eutectic $Ge_{15}Te_{85}$ alloy were constructed by combining density functional calculations with RMC. The resulting three models had equally good computational energies (as set by definition). However, the best fit to the experimental data was obtained with the structure which contained a small number of Ge-Ge bonds. The Ge-Ge bonds have been excluded from many models of the amorphous $Ge_{15}Te_{85}$ structure, and they can be considered as defects. Our results show that they should not be excluded from the model structures, as they seem to allow for a better fit with the experimental and computational ND structure factors while keeping the DF energy low.

Germanium has a coordination number between 3.5 and 4 in all structures, while tellurium is close to twofold coordinated. The most common local environments (neighbors) for germanium are Te_3 and Te_4, while the most common ones for tellurium are GeTe and Te_2. Tellurium is slightly overcoordinated with respect to the 8-N rule (N is the number of valence electrons), and germanium is undercoordinated.

The model structures of $Ge_{15}Te_{85}$ contain two types of germanium atoms. Approximately half of the germanium is fourfold coordinated with a distinct gap between first and second nearest-neighbors (in PDF). This is attributed to a tetrahedrally coordinated local bonding environment. Another half of Ge has a defective octahedral coordination with 3 short bonds, and there is no well-defined gap visible between the first and second-neighbor shells.

Another similar division can be made for tellurium by distinguishing the atoms that bind to germanium from those that only bind to other tellurium atoms. The latter type forms a threadlike mesh where the $GeTe_x$ bits reside, and there is no clear indication of segregation visible. However, the division to Ge-bonding and non-Ge-bonding tellurium could act as a precursor for segregation. It is also

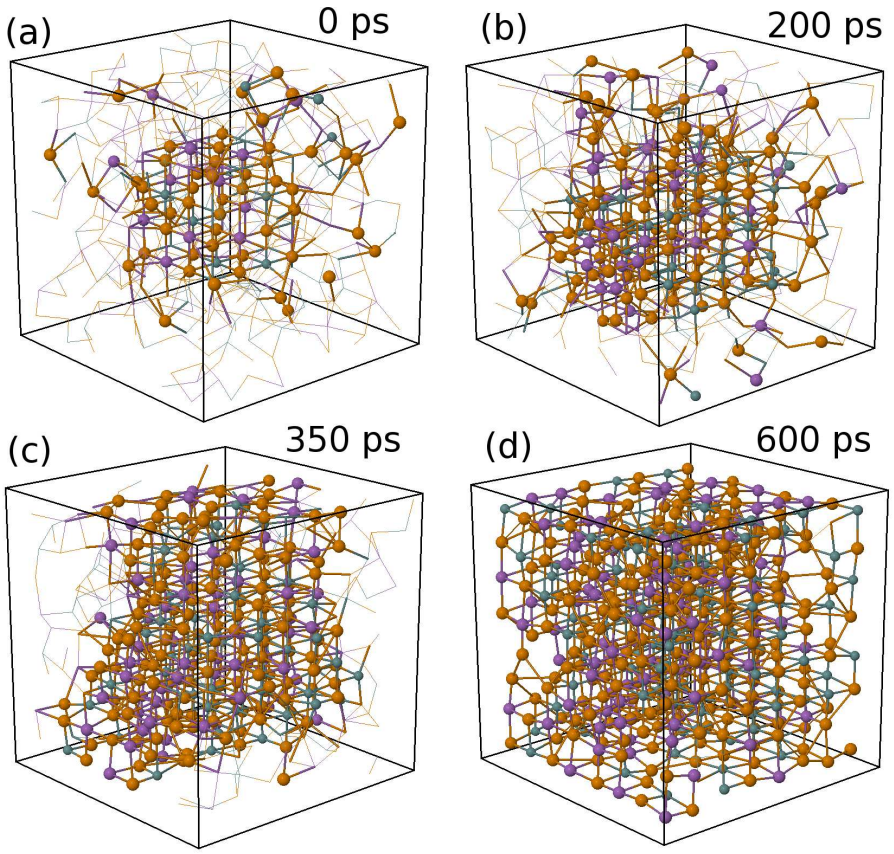

Figure 13: Visualization of the 600 K structure at different stages of crystallization. The atoms with crystalline environment are highlighted with balls and sticks and the fixed seed is visible in the first panel. Green: Ge, purple: Sb and orange: Te.

possible that the limited simulation cell size does not support segregation. The GeTe bits can form clusters, where the ABAB motif can be seen in ABAB rings. $Ge_{15}Te_{85}$ contains a significant volume of cavities (22-24%) and a number of large rings that surround the cavities.

5.3 Crystallization of $Ge_2Sb_2Te_5$

We studied the crystallization of $Ge_2Sb_2Te_5$ (GST) at constant temperatures with a fixed "seed" present in the otherwise amorphous structure. According to the CN theory (section 4.2), a material crystallizes by creating a crystallite of critical radius spontaneously from which the crystallization then proceeds according to the energy minimization principle. There are studies suggesting that the critical crystallite size for GST would be of the order of few tens of atoms [82]. We used a 64-site crystallite seed (lattice constant 3.0 Å) with 13 Ge, 13 Sb and 32 Te atoms (58 atoms, 6 vacancies) that followed a commonly accepted model where tellurium occupies one sublattice and Ge/Sb/vacancies randomly occupy the other. The function of the seed was to skip the stochastic part of the crystallization (the onset) and enable focusing on the growth of the crystal around the seed.

The seed was embedded into an amorphous structure from an earlier work

[47]. The super cell size was 24.629 Å (0.0308 atoms/Å^3) in the amorphous state, and the size was decreased in five steps of 0.114 Å each to 24.060 Å (0.0330 atoms/Å^3) during the simulations to mimic the density increase of a thin film sample. Three simulations with 460 atoms were done at 500, 600 and 700 K in order to study the temperature dependence of crystallization. The 500 and 600 K simulation lengths were 600 ps each with a full crystallization at 600 K (shown in fig. 13) and some early signs of order at 500 K. The 700 K simulation crystallized faster, and the simulation length was only 350 ps. In addition to these three simulations, one 600 ps simulation with 648 atoms and larger super cell was performed. However the potential crystalline structure would not have been commensurate with the simulation cell and number of atoms, and thus, crystallization was not expected. This simulation showed early signs of crystallization after which the crystalline fraction of atoms decreased. In this thesis I will concentrate on the three smaller simulations.

We analyzed the crystallization from the trajectory using a Steinhardt-type order parameter [83], where the vectors of atomic bonds are projected onto spherical harmonics basis $Y_{lm}(\mathbf{r}_{ij})$, and the local order can be calculated as

$$Q_{lm}(i) = \frac{1}{N(i)} \sum_{j=1}^{N(i)} Y_{lm}(\mathbf{r}_{ij}), \tag{46}$$

where $N(i)$ is the number of neighbors of atom i. This is then averaged over the atom i and its neighbors

$$\bar{Q}_{lm}(i) = \frac{1}{N_b(i)} \sum_{k=1}^{N_b(i)} Q_{lm}(k), \tag{47}$$

where $N_b(i)$ includes the atom i and its neighbors. The final order parameter is achieved by summing over m,

$$\bar{Q}_l(i) = \sqrt{\frac{4\pi}{2l+1} \sum_{m=-l}^{l} \left|\bar{Q}_{lm}(i)\right|^2}. \tag{48}$$

This scheme can be used to various crystal structure and symmetries by changing the l parameter, and for the cubic structures the first nonzero value of $\bar{Q}_l$ is when $l = 4$. Based on the trajectories of amorphous, crystallizing and crystalline samples of GST we define a "crystalline atom" as any atom which has $\bar{Q}_4 \geq 0.6$.

Percolation is the formation of long-range connections in a random lattice. Percolation has been found to affect electrical properties significantly in GST [84], as current only needs a narrow conducting pathway, but there is a negligible effect on optical properties, as reflectivity is measured as an average over finite-sized spherical laser spot. We calculate percolation properties in the simulations by determining if there is a continuous bonded path of crystalline atoms from any atom to its periodic replica. We use 3.20 Å bond length cutoff for this purpose. If such a path exists, then the atom (and consequently all the atoms belonging to the

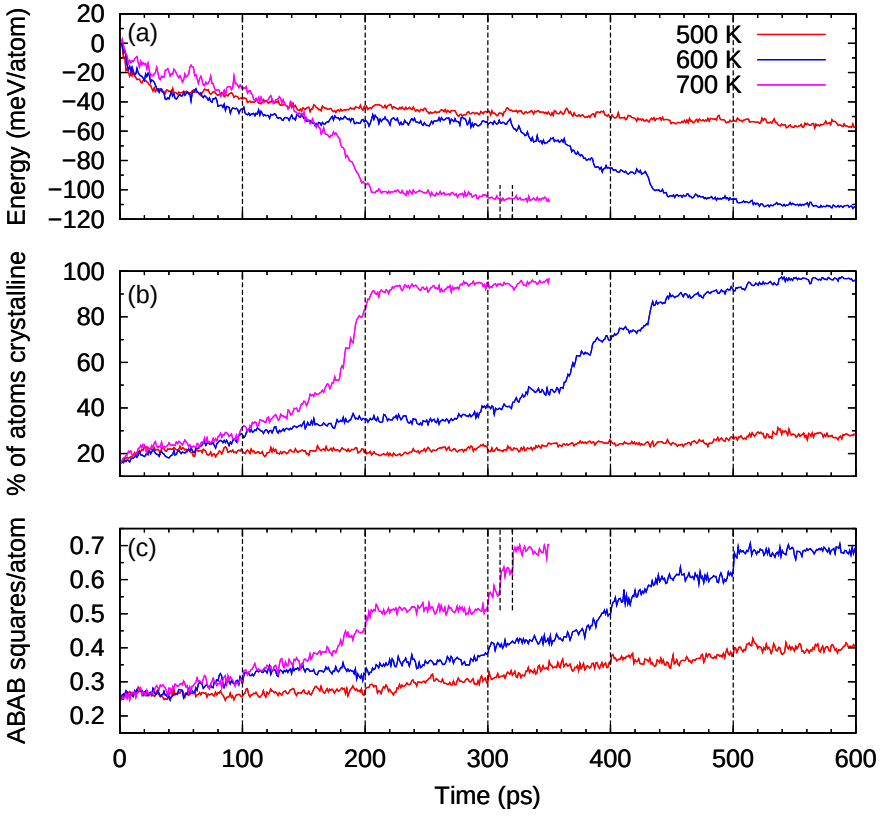

Figure 14: (a) Total energy (normalized for box size), (b) fraction of crystalline atoms, and (c) number of ABAB rings/atom in each simulation. The vertical dashed lines mark reductions in the super cell size until the crystalline density is reached.

bonded crystalline cluster) are considered percolating. In practice, the relatively large size of the seed (half of the super cell width in 1D, quarter of the area in 2D) makes it probable that a percolating path would go through the seed or the crystalline cluster surrounding it. This means that after the very beginning of the simulation, there is only one crystalline cluster (comprising the seed and the attached crystalline atoms) which is then the percolating system.

5.3.1 Crystallization overview

The simulation energy in all three simulations, shown in figure 14(a) follows inversely the fraction of crystalline atoms in figure 14(b). The 700 K simulations crystallizes most rapidly, which is in agreement with recent ultrafast calorimetry measurements [52], where the peak crystallization speed was found at approximately 670 K temperature. The crystallization is most rapid from 150 ps to 200 ps at 700 K and at 600 K from 325 ps to 450 ps. Prior to the fast crystallization phase, the crystalline fraction increases steadily, and the fast crystallization begins after approximately 40% of the atoms are crystalline.

The number of ABAB squares per atom is shown in figure 14(c) and it follows the crystalline fraction evolution. However, the number of ABAB rings seems to

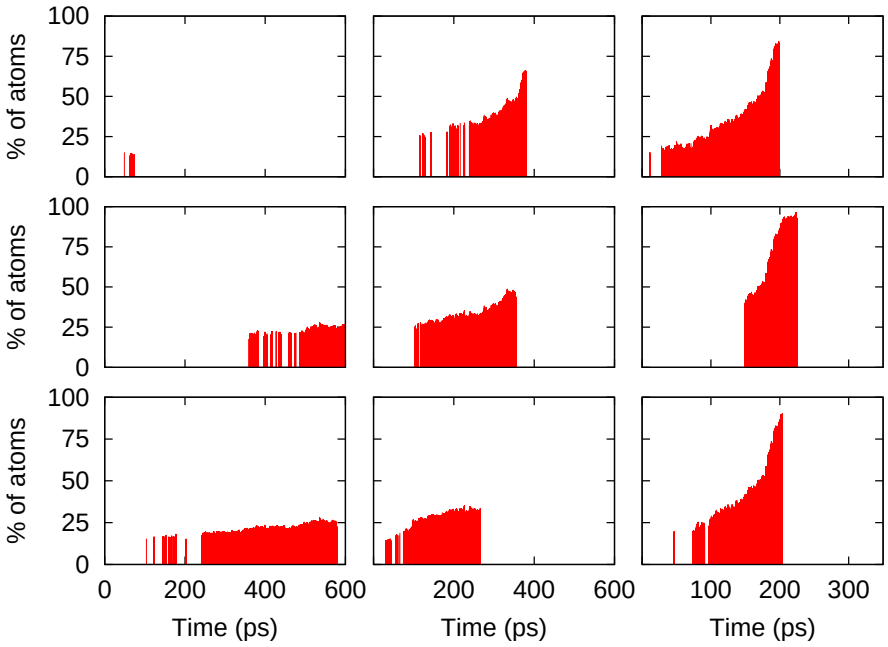

Figure 15: Size of the percolating crystalline cluster as a function of time. Left, middle and right columns are 500, 600 and 700 K simulations, respectively. Top, middle and bottom rows are percolation along x, y and z axes, respectively.

be sensitive to the super cell size. The number of ABAB squares shows a sudden jump as the super cell size changes. Especially, this can be observed in the 600 K simulation at 500 ps and in the 700 K simulation after 200 ps. This could be due to the restrictions of the definition of an ABAB ring, a bond length cutoff of 3.2 Å was used here requiring that all four bonds of an ABAB square were below this value. It is easy to imagine based on the crystalline structure that the network of ABAB rings will break in all possible directions if the super cell size becomes too large. This is then reflected in the average number of ABAB squares, which seems to have a capping limit based on the super cell size.

The order parameter $\bar{Q}_4$ does not have this behavior, and there are no sudden jumps visible at the changes in super cell size. This can be explained by noting that too long bonds do not affect the calculation of $\bar{Q}_4$: A removal of a bond does not change the crystallinity of an atom if the bond angles where the removed bond contributed were similar to the angles of the other bonds.

5.3.2 Bonds and connectivity changes

The crystallization process is shown in figure 13, which shows snapshots of the 600 K structure during the crystallization. The crystallization starts from the seed as expected, and the crystalline cluster starts to percolate quite early in the simulation. Percolation is visible in the straight edges of the highlighted structure. The crystallization is complete at 600 ps, but there are still lattice defects with missing atoms and atoms in wrong sublattice visible around the edges of the simulation cell.

The percolation is shown in figure 15, the graphs show the percolating cluster

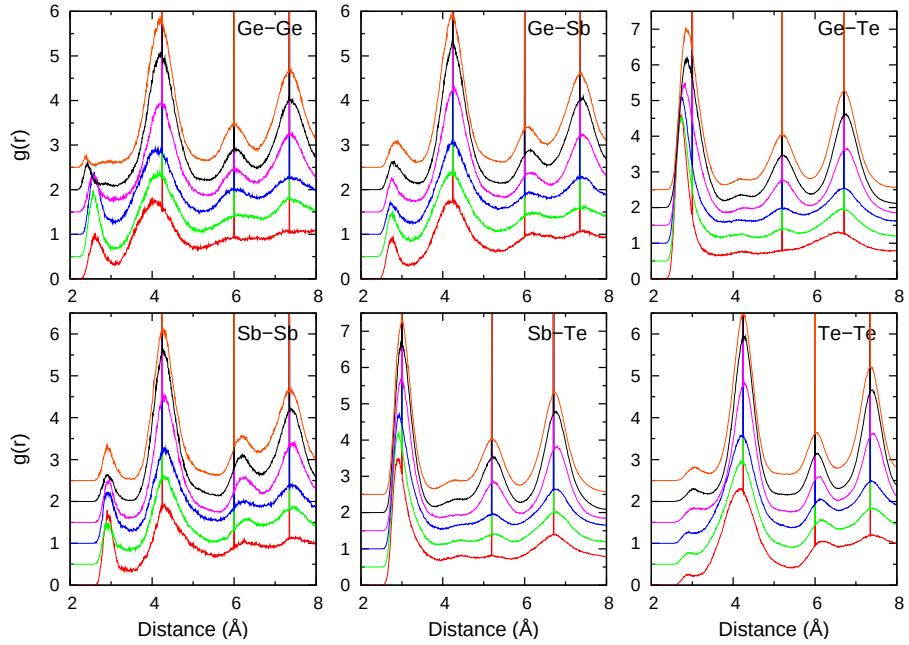

Figure 16: PDF of atom pairs in the 600 K simulation. Each plot is the average over 20 ps of trajectory. Red: 80-100 ps, green: 180-200 ps, blue: 280-300 ps, magenta: 380-400 ps, black: 480-500 ps, and orange: 580-600 ps. Successive plots are shifted by 0.5. The vertical lines arise from the crystalline seed with a lattice constant 3.0 Å.

size whenever there is percolation in one or more of the coordinate directions. The shapes of the graphs are identical for different directions towards the end of each simulation, as the percolating cluster is the same for every direction. The order of percolation directions is z, y, and x at 600 K, and x, z, and y at 700 K. This means that there is no preferred direction found for percolation, even though all the simulations were started from the same starting structure. The percolation is also present in the 500 K simulation in two (y and z) directions even though the crystalline fraction is below 30% at the end of the simulation. It is seen that as little as 20% crystalline fraction can enable a stable percolation connection.

The partial PDFs of 600 K simulation are shown in figure 16, and they show the evolution of the bonding network during the crystallization. The Bragg peaks from fixed seed are visible at various distances corresponding to 3.00 Å lattice constant and different diagonal lines within such lattice (3.00, 4.24, 5.20, 6.00, 6.71 and 7.35 Å). During crystallization, the free-moving atoms gather weight around these peaks as the structure crystallizes, and the crystallization seems to be fastest between 280-300 ps (blue) and 480-500 ps (black) lines. The peaks between 2 and 3 Å in the so-called wrong bond pairs (Ge-Ge, Ge-Sb, Sb-Sb and Te-Te) diminish and move to higher distances but do not vanish completely.

This is also visible from the evolution of the number of wrong bonds shown in figure 17. In the simulations where crystallization is complete (600 and 700 K), the number of wrong bonds decreases the most, while there is little change in the 500 K simulation. When looking at the specific atom pairs, it is seen that Te-Te bonds are the most numerous, and this can be explained at least in part by the

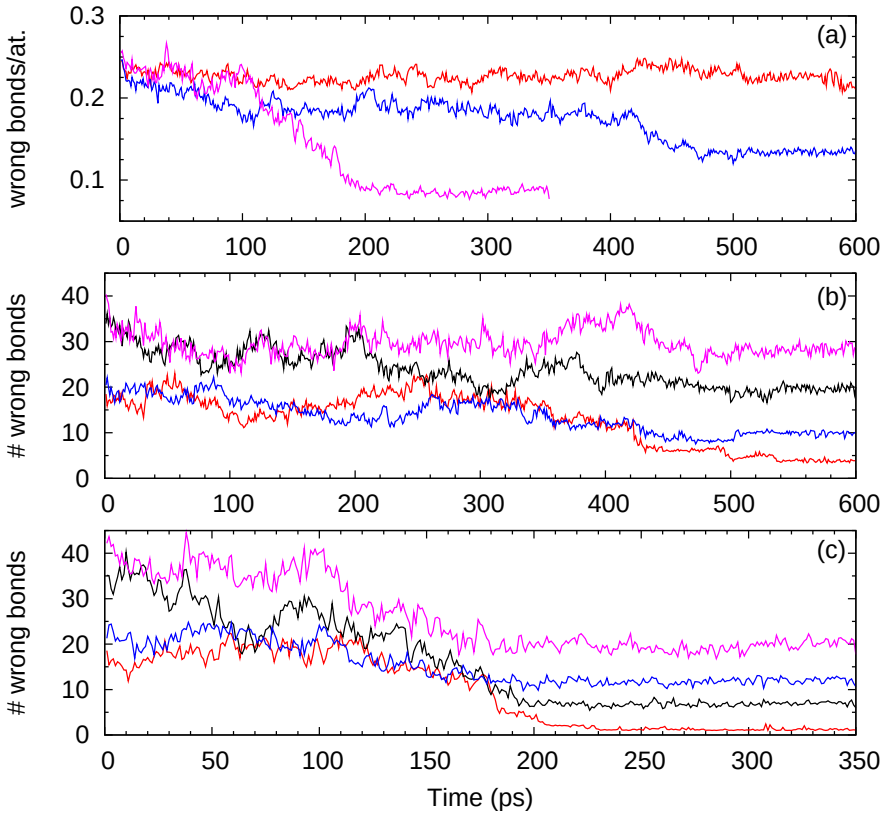

Figure 17: (a) Average number of wrong bonds per atom (all simulations). (b) Number of wrong bonds by type at 600 K and (c) 700 K simulations. In (a) red: 500 K, blue: 600 K, and magenta: 700 K. In (b) and (c): red: Ge-Ge, black: Ge-Sb, blue Sb-Sb, and magenta: Te-Te.

abundance of tellurium atoms in the structure. However, the difference between Ge-Ge and Sb-Sb bonds [red and blue lines in (b) and (c)] cannot be explained in terms of composition as there are equal numbers of these atoms. Also the number of Ge-Sb bonds is higher than the number of Sb-Sb bonds at 600 K but the opposite is true for 700 K. The reason for this could be the temperature, but one cannot make solid conclusions based on only two simulations. Overall, the number of wrong bonds goes down as the structure crystallizes, but a number of wrong bonds are still present at the fully crystalline structure. A possible reason for this is that the rapid rate of crystallization does not support ordering to a perfect lattice for all atoms.

Figure 18 shows the PDFs involving cavities before and after crystallization. The center point of a largest sphere that can be placed inside a cavity without overlapping any atoms was used as the cavity center point here. There is a clear tendency for the cavity centers to move away from Ge and Sb nearest-neighbor lattice distance (3.00 Å) and towards the diagonal site at 4.24 Å distance. For Te, the cavities remain at 3.00 Å distance, but there is some oscillation visible, similar oscillation can be seen at the Ge-cav and Sb-cav PDF near 6.00 Å. In addition to changes induced by the changing super cell size, the total volume of cavities fluctuates during the simulation (see sec. 5.3.4), and this can be related to the PDF

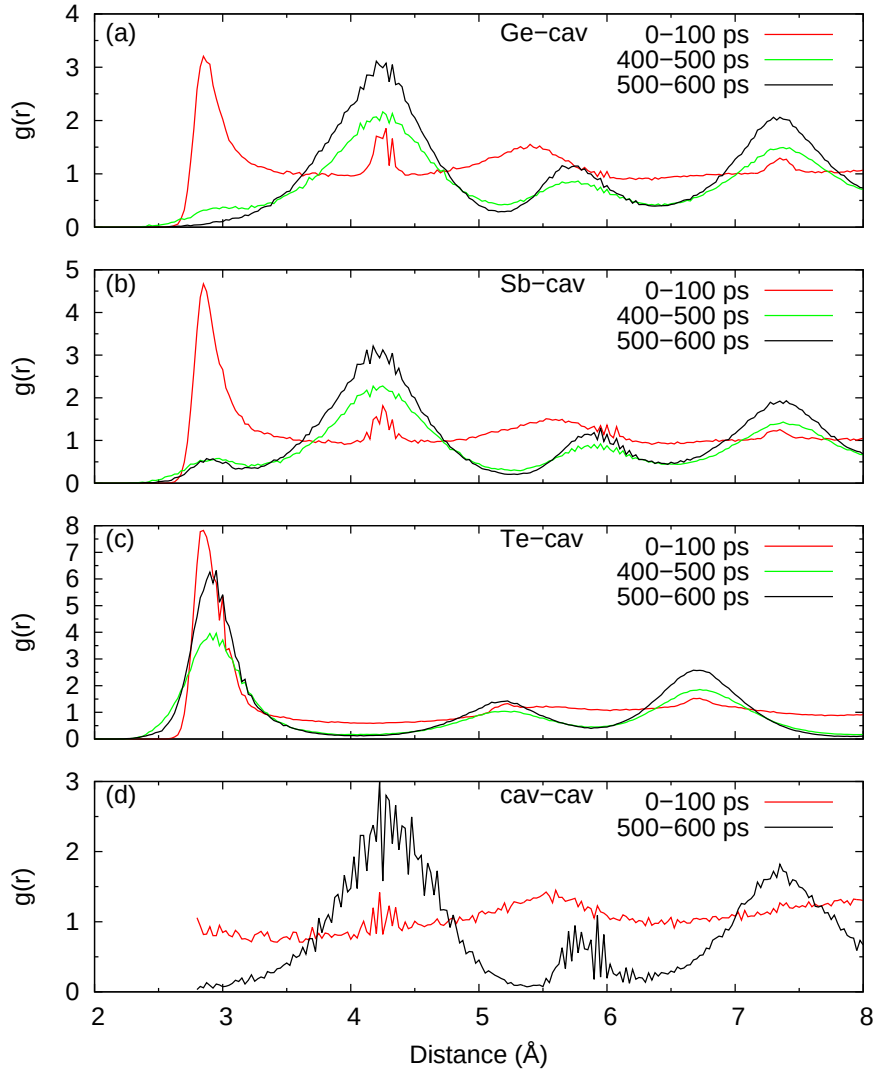

Figure 18: Partial PDF involving cavities (cav) in the 600 K simulation. (a) Ge-cav, (b) Sb-cav, (c) Te-cav, and (d) cav-cav. Red: Average over 0-100 ps, blue: average over 400-500 ps, and black: average over 500-600 ps. Note the different scales.

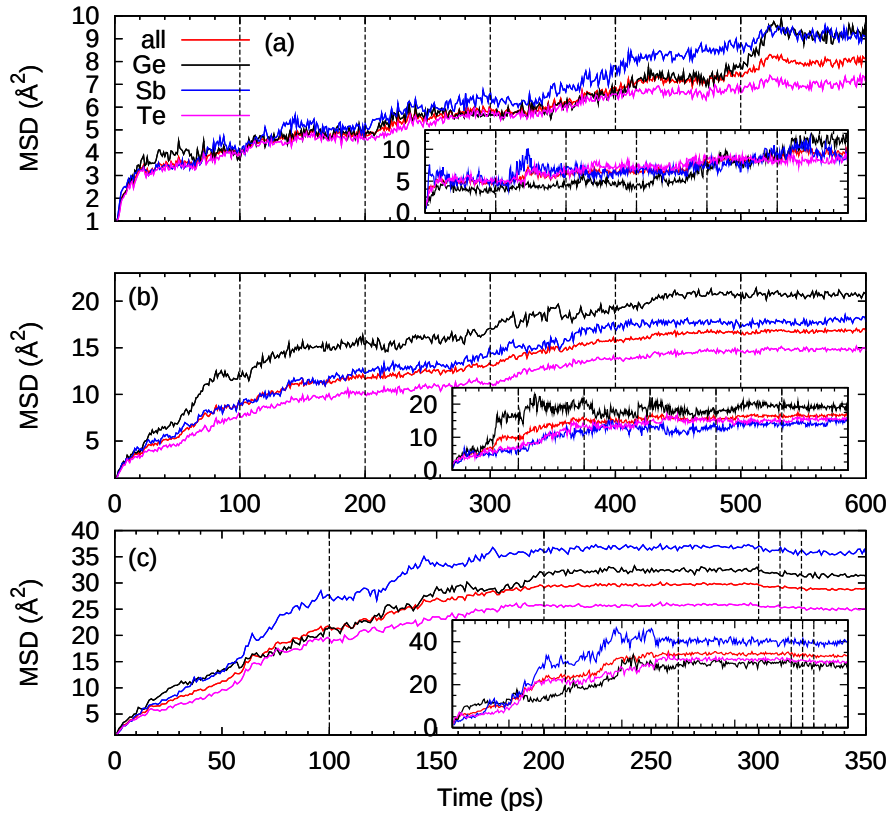

Figure 19: MSD for all atoms and for each element at (a) 500, (b) 600 and (c) 700 K. Insets show σ(MSD)/MSD. Fixed atoms were excluded.

fluctuations.

5.3.3 Atomic mobility

Atomic motion was studied based on the mean-square-displacement (MSD) of free moving atoms, which is shown in figure 19. The MSD increases until the crystallization locks the atoms in a lattice (600 K and 700 K) and seems to continue until the end of the simulation at 500 K, where the structure did not crystallize yet. It is notable in the 500 K simulation that the germanium MSD rapidly increases after 500 ps up to the antimony MSD which was higher until then. The order of germanium and antimony MSD are the opposite at 600 and 700 K, and it is known that antimony has a higher mobility in the liquid, and the behavior at higher T could be related to this property. The insets show the relative deviation, σ(MSD)/MSD, and they indicate a wide range of different mobilities for atoms. This is understandable as some atoms that crystallize in the first shell around the fixed seed do not move much during the simulation, whereas other atoms that crystallize at the edge of the simulation box can diffuse for much longer until they are locked in the lattice. In both, the 600 K and 700 K simulations, the atom species that is the most mobile also has the highest σ(MSD)/MSD, while the atom species that is second most mobile has the lowest σ(MSD)/MSD.

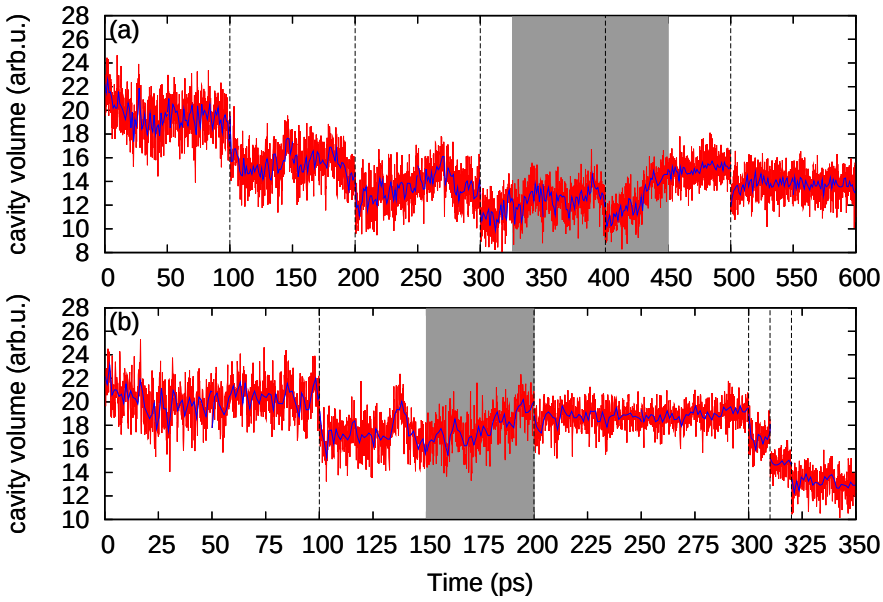

Figure 20: Variation of total cavity volume in (a) 600 and (b) 700 K simulations, blue line is average over 1 ps period. Shaded areas correspond to the periods of fastest crystallization [325-450 ps in (a) and 150-200 ps in (b)].

5.3.4 Cavities

Cavities play an important role in the crystallization mechanics. The total volume of cavities is shown in figure 20, and it shows a decrease of ~30%. Based on the cavity fractions of crystalline and amorphous GST and the density change associated with crystallization, this is in agreement with the expected change. Most of the change in cavity volume comes from the jumps at super cell size changes but there is some variation within a single-cell-size simulation periods, for example between 400-500 ps at 600 K which coincides with the sudden increase in the crystalline fraction at 430 ps (see fig. 14). This variation in the cavity volume could cause the oscillation seen in the Te-cav PDF (fig. 18) where the peak at 3.0 Å decreases from 0-100 ps to 400-500 ps and increases again at 500-600 ps.

The distribution of cavities is both random and uniform, and no preferred regions could be distinguished where cavities were more abundant than elsewhere. The cavity size distribution is shown in figure 21. It shows that the cavity distribution before the crystallization resembles the liquid phase. The 600 K simulation has a clear peak near 80 Å^3, which was tracked down to a dual cavity (di-vacancy) inside the fixed seed. The distribution after crystallization shows periodic peaks at multiples of ~35 Å^3, which is approximately the volume of a single vacancy in the crystalline structure. These peaks thus arise from different sizes of lattice vacancies which comprise 10% of the lattice.

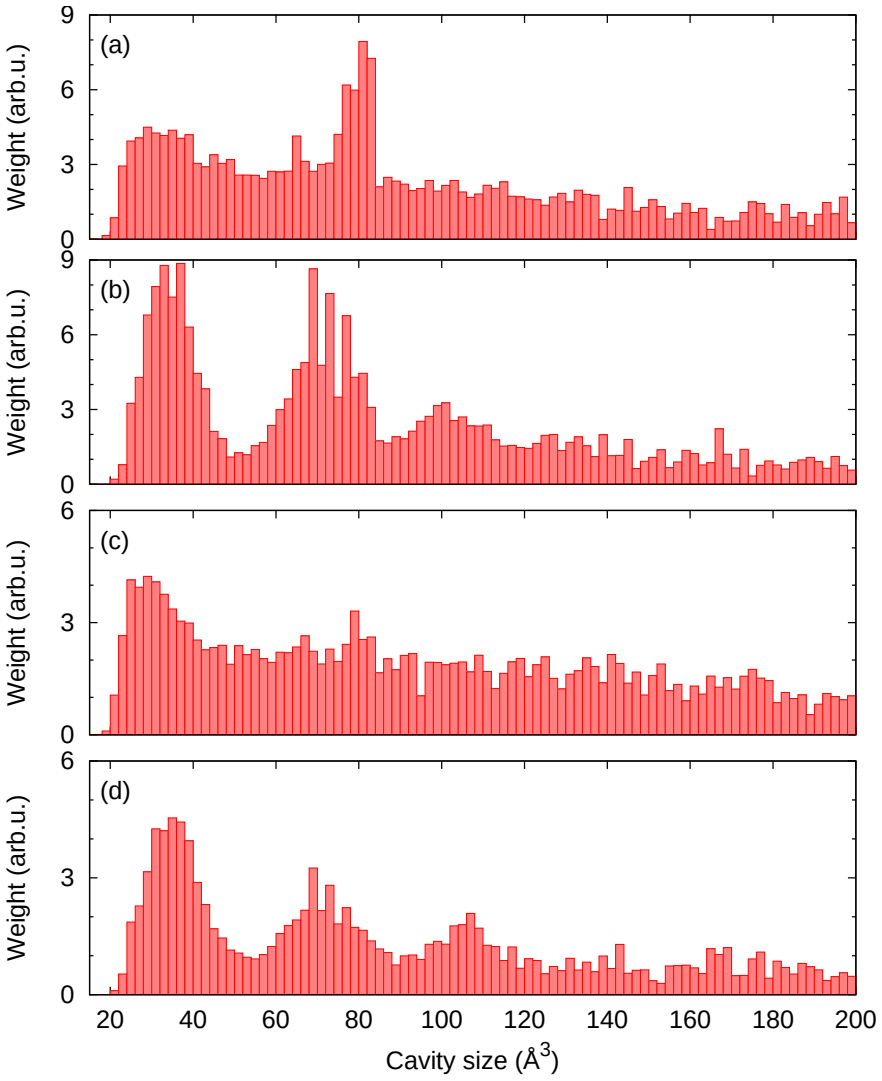

Figure 21: Cavity size distribution weighted by the cavity volume at 600 K: (a) before (0-50 ps) and (b) after crystallization (550-600 ps), and at 700 K: (c) before (0-50 ps) and (d) after crystallization (320-350 ps).

5.3.5 Conclusions

The crystallization of $Ge_2Sb_2Te_5$ was studied in different temperatures with the focus on the late part of the crystallization. Crystalline growth was seen in all structures, but at 500 K the structure did not fully crystallize. At 600 K and 700 K, the crystallization was complete before 600 ps.

These simulations of $Ge_2Sb_2Te_5$ show that percolation of the crystalline cluster is present from very early on in the crystallization process. It requires as little as a 20% crystalline fraction for the percolation to occur continuously, and it appears as the formation of narrow necks between periodic replicas of the seed. The crystallization speed in our simulations is higher at 700 K than at 600 K, which is in agreement with recent ultrafast DSC study by Orava *et al.* [52] where the peak crystallization speed was observed at 670 K.

Wrong bonds in the crystalline structure seem to be an inherent consequence of the very rapid crystallization. Their numbers decrease from the amorphous values, but there is a small number of wrong bonds left in the fully crystalline structure. Cavities are generally assumed to play an important role during the crystallization of GeTe-Sb_2Te_3 pseudobinary materials, and our simulations suggest that cavities provide space for atomic rearrangements during the crystallization. They also order in the end of the crystallization with a small number of cavities remaining in the wrong lattice site, at 3 Å distance from Sb atoms. Some fluctuations in the cavity volume was seen, and it is possible that these fluctuations results in from atoms, which temporarily occupy vacancies in order to facilitate rearrangements to reduce the number of wrong bonds in the nearly crystallized structure.

5.4 Structures of GaSb and $GaSb_7$

The structures of GaSb and $GaSb_7$ were studied in the third article, in particular the differences between as-deposited (AD) and melt-quenched (MQ) structures. The aim of this study was to find the first detailed structural models of both amorphous polymorphs and of each composition. The model AD structures were created by iteratively relaxing twenty 24-atom layers (sparse layers, 3.2 Å min. inter-atomic distance) on top of a random 48-atom fixed template (2.6 Å min. inter-atomic distance) and compressing the resulting film structure into a bulk as-deposited structure in a piston-like manner (but with small pressure). The final models had 528 atoms each and a "vacuum" of at least 10 Å was used to separate the films in vertical direction.

The procedure is shown in figure 22(a). The deposited layers were allowed to relax for 5 ps at 300 K, and in few cases additional relaxation was required, particularly with the Sb-rich $GaSb_7$ where the deposition resulted in isolated Sb_4 tetramers (the most stable cluster size for Sb). Figures 22[(b)-(c)] show the GaSb and $GaSb_7$ film structures and the corresponding compressed AD structures. The $GaSb_7$ film was very porous, which is visible in the figure 22(c). The $GaSb_7$ film also contracted significantly more during the compression than the GaSb film. In the beginning of the compression, the extra vacuum was removed by decreasing the simulation cell size in the z-direction until the shortest distance between atoms on top and bottom of the film was 3.5 Å. The compression was nonlinear, and we

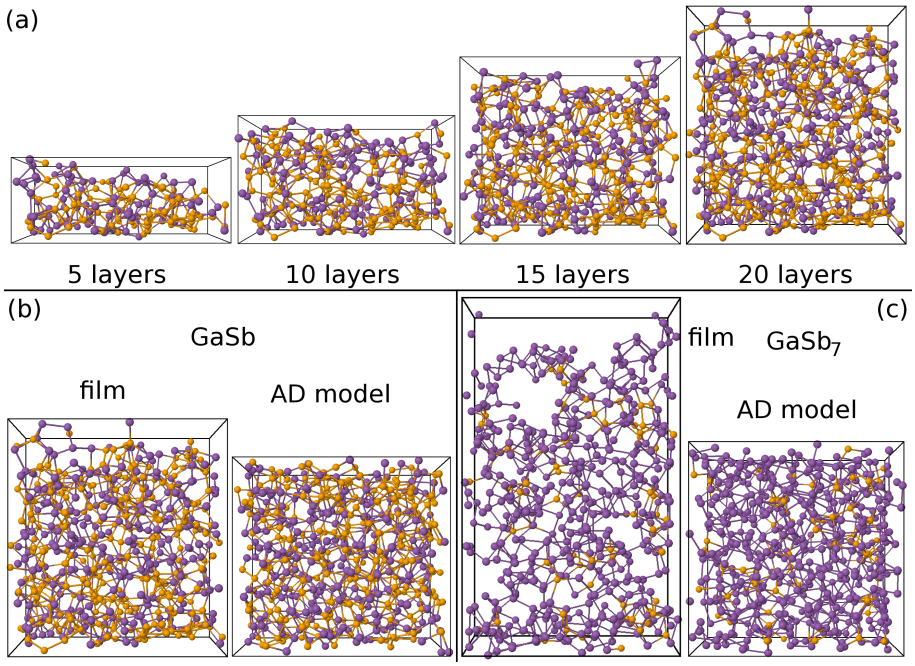

Figure 22: The growth of the GaSb film: Fixed layer with 5, 10, 15 and 20 relaxed layers (a), GaSb film structure and compressed AD structure (b), and $GaSb_7$ film structure and compressed AD structure (c). Orange: Ga, purple: Sb.

started with higher compression rates (at most 0.5 Å/ps) since the sparsely spaced atoms could move easily, and gradually slowed the process to 0.067 Å/ps to allow for a better relaxation of the structure.

The model structure for melt-quenched (MQ) structure was created from the AD structure by heating it up above the melting temperature (GaSb to 1000 K, $GaSb_7$ to 900 K), and cooling it down rapidly to produce the amorphous structure. These simulations were 60 ps for both alloys. The densities had initially been approximated with known bulk densities of c-GaSb and c-Sb, and we verified that they were reasonable by evaluating computational stress tensor values during MD.

5.4.1 Bonds and coordination numbers

The final as-deposited (AD) and melt-quenched (MQ) structures of GaSb are shown in figures 23[(a)-(b)] with close-ups of small bits of the structure in [(c)-(d)]. The simulated PDF and $S(Q)$ are shown in figure 24. The XRD PDF has been experimentally measured by Shevchik and Paul on GaSb films deposited on Cu substrates [85], and their PDF has similar values (2.67±0.03 Å, 4.30±0.05 Å) for the first two peaks as our structures (AD: 2.68 and 4.32 Å, and MQ: 2.70 and 4.36 Å, for total PDF with XRD weights).

Ga-Sb bonds are the most abundant in both structures. The PDF weight for both homopolar bonds decreases from AD to MQ, while the weight of the Ga-Sb bond increases. This is also visible in the partial coordination numbers (table 5), and the crystalline GaSb (where no homopolar bonds exist outside of

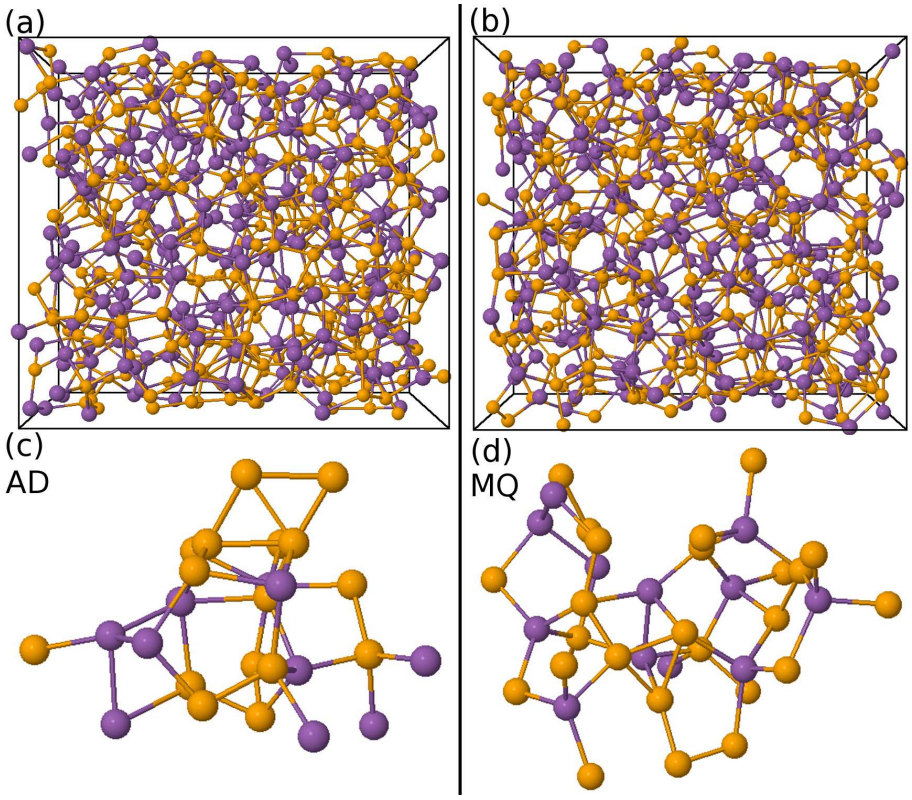

Figure 23: Full structures (a-b) and close-ups of structural details (c-d) for GaSb. AD structure in (a) and (c) and MQ structure in (b) and (d). Orange: Ga, purple: Sb.

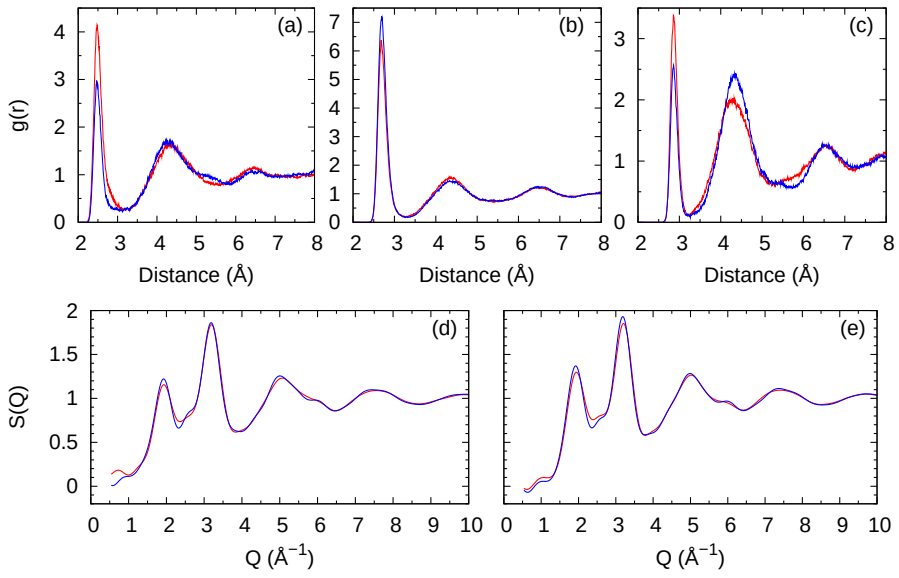

Figure 24: PDF of GaSb for atom pairs Ga-Ga (a), Ga-Sb (b), Sb-Sb (c) and S(Q) calculated with ND weights (d) and XRD weights (e). Red: AD, blue: MQ.

Table 5: First maxima ($r^{\mathrm{max}}_{\mathrm{X-Y}}$) and minima ($r^{\mathrm{min}}_{\mathrm{X-Y}}$) in the partial PDF (Å), coordination numbers N_r for the corresponding r^{min}, and chemical coordination numbers N_c.

	GaSb		$GaSb_7$	
Structure	AD	MQ	AD	MQ
$r^{\mathrm{max}}_{\mathrm{Ga-Ga}}$	2.48	2.47	2.48	2.46
$r^{\mathrm{max}}_{\mathrm{Ga-Sb}}$	2.68	2.69	2.67	2.69
$r^{\mathrm{max}}_{\mathrm{Sb-Sb}}$	2.86	2.86	2.88	2.89
$r^{\mathrm{min}}_{\mathrm{Ga-Ga}}$	3.20	3.13	2.82	2.92
$r^{\mathrm{min}}_{\mathrm{Ga-Sb}}$	3.28	3.27	3.25	3.24
$r^{\mathrm{min}}_{\mathrm{Sb-Sb}}$	3.19	3.27	3.18	3.19
N_r (Ga)	4.35	4.11	4.01	3.98
N_r (Sb)	3.87	3.95	3.20	3.19
$n_{\mathrm{Ga-Ga}}$	1.73	1.13	0.19	0.12
$n_{\mathrm{Ga-Sb}}$	2.62	2.98	3.82	3.86
$n_{\mathrm{Sb-Ga}}$	2.62	2.98	0.55	0.55
$n_{\mathrm{Sb-Sb}}$	1.25	0.97	2.65	2.64
N_c (Ga)	3.98	3.93	3.95	3.94
N_c (Sb)	3.79	3.85	3.15	3.18
$n^{\mathrm{chem}}_{\mathrm{Ga-Ga}}$	1.44	1.02	0.21	0.12
$n^{\mathrm{chem}}_{\mathrm{Ga-Sb}}$	2.54	2.91	3.74	3.82
$n^{\mathrm{chem}}_{\mathrm{Sb-Ga}}$	2.54	2.91	0.53	0.55
$n^{\mathrm{chem}}_{\mathrm{Sb-Sb}}$	1.25	0.94	2.62	2.63

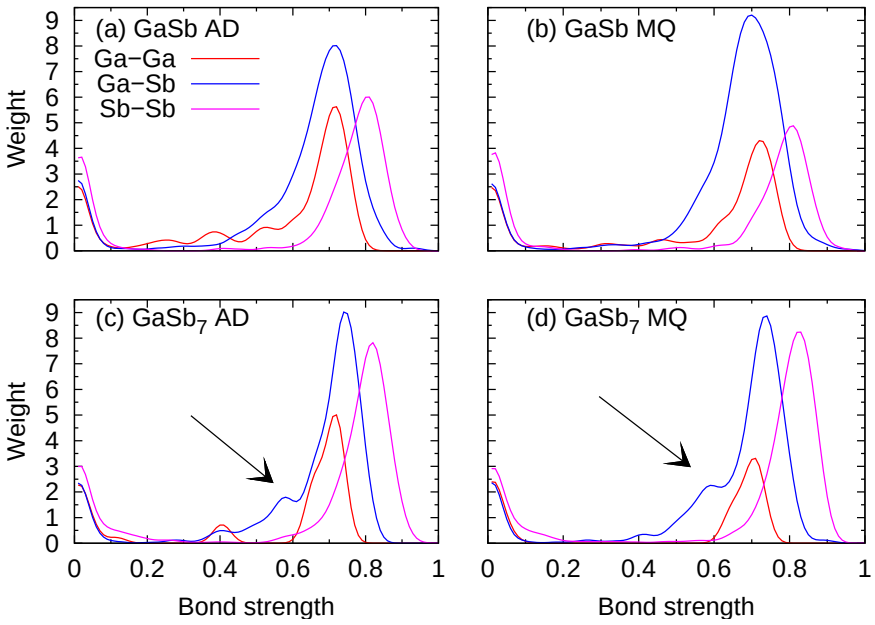

Figure 25: Chemical bond strengths in GaSb and $GaSb_7$. The arrows mark local maxima at 0.6 corresponding to fourfold Sb.

Table 6: Nearest-neighbor composition (atomic %, configurations with population < 1.5 % in all structures are not listed) of amorphous GaSb and $GaSb_7$ using a chemical bond order cutoff 0.3 for counting bonds. The total weight for a particular coordination is given in boldface.

			GaSb		$GaSb_7$	
Atom	Coordination	Neighbors	AD	MQ	AD	MQ
Ga	**5**	Ga_4Sb	1.9	0.8	-	-
		Ga_3Sb_2	3.8	3.4	-	-
		Ga_2Sb_3	1.5	1.1	-	-
		All	**8.0**	**5.3**	**1.5**	-
	4	Ga_3Sb	9.5	2.7	-	-
		Ga_2Sb_2	17.8	15.5	-	-
		$GaSb_3$	37.5	37.5	13.6	12.1
		Sb_4	15.5	27.3	78.8	81.8
		All	**81.1**	**83.0**	**92.4**	**93.9**
	3	$GaSb_2$	5.7	4.9	3.0	-
		Sb_3	2.3	4.6	1.5	6.1
		All	**10.6**	**11.4**	**6.1**	**6.1**
Sb	**5**	Ga_5	4.6	2.7	-	-
		All	**4.6**	**4.2**	**0.2**	-
	4	Ga_4	14.4	24.6	-	-
		Ga_3Sb	30.7	34.5	1.5	0.9
		Ga_2Sb_2	21.2	14.8	4.6	7.8
		$GaSb_3$	3.8	1.5	6.9	5.6
		Sb_4	-	-	2.0	3.3
		All	**70.1**	**75.4**	**14.9**	**17.5**
	3	Ga_3	3.0	4.6	0.2	0.4
		Ga_2Sb	8.7	9.1	4.8	3.0
		$GaSb_2$	11.0	4.9	22.3	23.4
		Sb_3	2.7	1.5	57.6	55.4
		All	**25.4**	**20.1**	**84.9**	**82.3**

defects) is in this regard closer to the MQ structure than AD structure. The coordination numbers were calculated from the atomic structure using a cutoff radius of 3.2 Å (N_r) and from bond orders using a cutoff bond strength of 0.3 (N_c). The bond orders (bond strengths) were calculated by projecting the Kohn-Sham eigenfunctions onto atomic *s*- and *p*-orbitals. The projection is 99.0-99.2% complete, depending on the structure. The cutoff bond strength was lower than the one used for $Ge_{15}Te_{85}$ because here the strongest-bond peaks continued to lower strengths in an oscillating manner (see fig. 25).

The coordination numbers of GaSb show a general fourfold coordination for both atomic species. The chemical coordination numbers are consistently slightly lower than the structural, although the PDF minimum distances are close to the cutoff radius. The overall tetrahedral coordination, visible in figure 23[(c)-

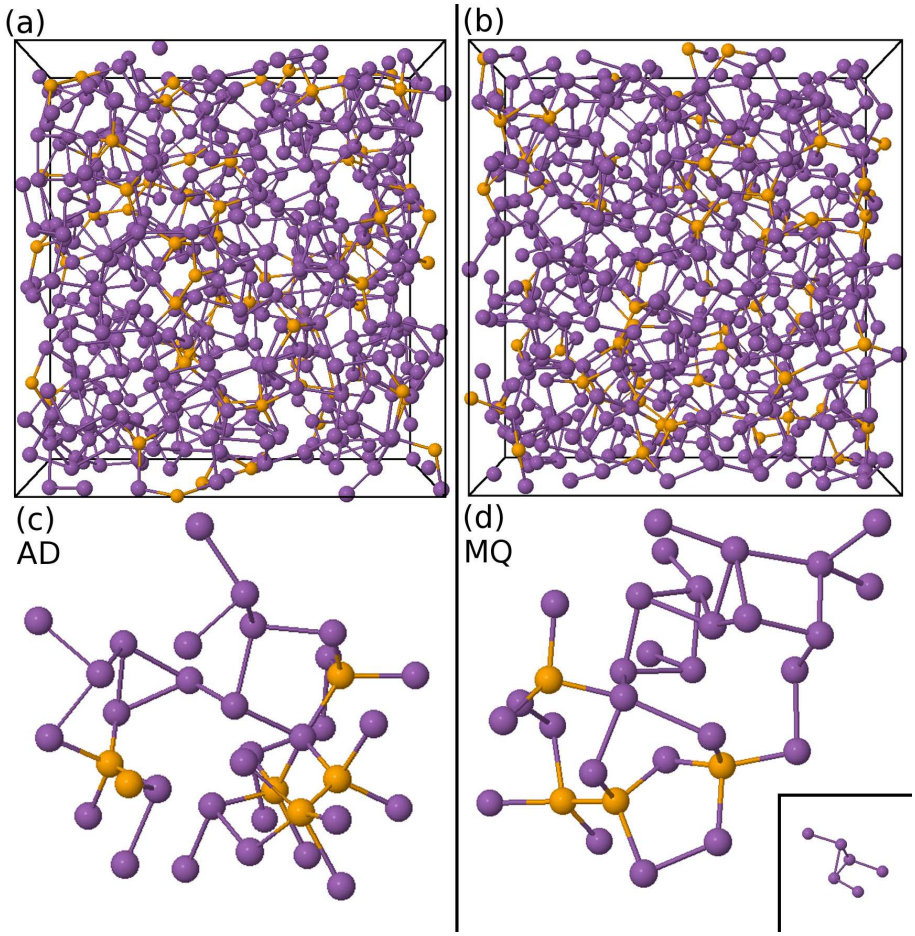

Figure 26: Full structures (a-b) and close-ups of structural details (c-d) for $GaSb_7$. AD structure in (a) and (c) and MQ structure in (b) and (d). Orange: Ga, purple: Sb.

(d)], is evident from the total coordination number for both Ga and Sb, which are approximately four for both AD and MQ structures. The nearest-neighbor composition is shown in table 6, and it shows that over 80% of gallium and 70% of antimony have four bonded neighbors in both structures. Fourfold coordination also increases from AD to MQ, and other changes include a decrease in threefold coordinated antimony and a slight increase in threefold coordinated gallium. When going from AD to MQ, gallium tends to switch to fewer gallium (more antimony) as neighbors, while antimony tends to move towards more gallium (less antimony) as neighbors.

The full model structures of $GaSb_7$ are shown in figures 26[(a), (b)], and the close-ups of the atomic bonding are shown in panels (c) and (d). The PDFs in figure 27[(a)-(c)] show that the number of Ga-Ga bonds decreases from AD to MQ. The absolute change is only of the order of 0.10 in the Ga-Ga coordination (table 5), but the relative change halves the Ga-Ga coordination. Otherwise, there are almost no changes in the PDFs. It is noted that the first v-shaped minima for Sb-Sb is similar to the one in AIST, which was attributed to the defective octahedral 3+3 coordination in ref. [87].

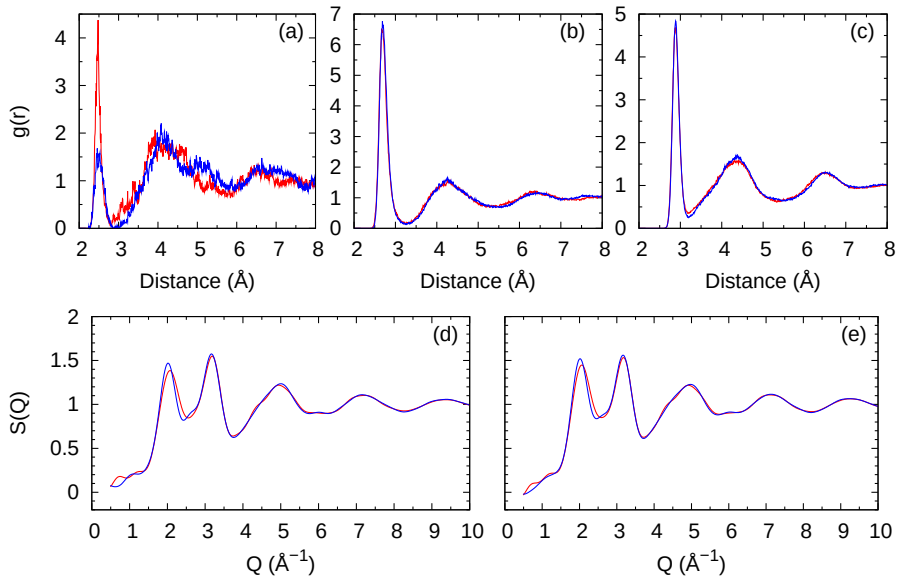

Figure 27: PDF of $GaSb_7$ for atom pairs Ga-Ga (a), Ga-Sb (b), Sb-Sb (c) and S(Q) calculated with ND weights (d) and XRD weights (e). Red: AD, blue: MQ.

The $GaSb_7$ coordination numbers listed in table 5 suggest an overall tetrahedral coordination for gallium and threefold defective octahedral coordination for antimony. These motifs are visible also in the structure close-up visualizations in figures 26[(c), (d)]. The chemical coordination numbers are closer to the structural ones than was the case for GaSb, and there is no similar systematic difference between the two for $GaSb_7$. The local environments in table 6 further support the tetrahedral gallium coordination (92-94% fourfold coordination), and threefold antimony coordination (82-85%), and the local environment statistics are almost identical for AD and MQ. The S(Q) shown in figures 27[(d), (e)] changes very little from AD to MQ: There is some change at FSDP region (~1 Å^{-1}) and on the height and depth of the first maxima and minima.

The bond order distribution of GaSb is shown in figures 25[(a)-(b)], and the main peak of nearest-neighbor bonds was between 0.5 and 0.9, but Ga-Ga bonds show some oscillation down to 0.3 in the AD structure. Most of the bonds are thus slightly weaker than a covalent single bond, which would correspond to a bond strength of unity. The bond strengths were calculated for the AD and MQ structures of $GaSb_7$ similarly as for GaSb. These graphs are shown in figures 25[(c)-(d)]. The Ga-Sb bond peak is narrower than the same peak of GaSb, and the Sb-Sb peak is higher due to the higher Sb fraction. There are some peculiar shoulders and minor maxima between the first and second nearest-neighbors, and these require a closer look. The maxima in the Ga-Ga graph of AD structure is from a single bond, and it stands out only because there are very few Ga-Ga bonds in $GaSb_7$. The local maxima in both of the Ga-Sb graphs (marked with arrows) near 0.6 bond strength turned out to be more interesting. The atom pairs forming these weaker bonds are often both tetrahedrally coordinated and form five-membered rings which go through the weak bond. This is visualized in figure 28(a) where the Ga-Sb pair is in the center with two five-membered rings that contain the

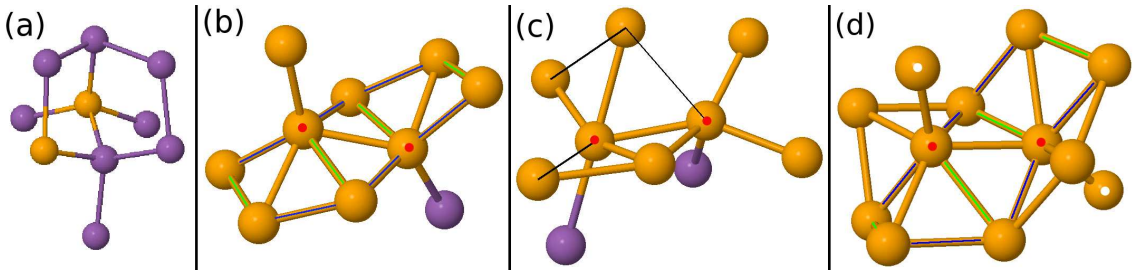

Figure 28: Tetrahedrally coordinated Ga and Sb atoms in $GaSb_7$ (a), atomic clusters in GaSb similar to crystalline gallium in AD (b) and MQ (c), and a closeup of the c-Ga structure corresponding to the cluster in AD GaSb (d). Black lines: long bonds (3.03 Å), orange: Ga, purple: Sb. Red dots denote hub atoms, blue lines stronger bonds and green lines weaker bonds.

weak bond and also a separate six-membered ring. Fourfold coordination of antimony is not so common in general (AD: 15%, MQ: 17.6%, see tab. 6), whereas 93% in AD and 97% in MQ of these weakly bonded antimony atoms are fourfold coordinated. A significant fraction (~40%) of all fourfold coordinated antimony atoms are weakly bonded.

The AD structure of GaSb contains an interesting detail: A cluster which shows striking visual resemblance to crystalline structure of gallium [86]. It consists of nine gallium atoms and one antimony atom, and it is visualized in figure 28(b) with the corresponding portion of crystalline gallium shown in the panel (d). The cluster is a slightly twisted sheet with two perpendicularly protruding atoms. The red dots in the figures denote a hub atom (six-coordinated in AD GaSb). In the gallium crystal structure the sheet is more bent, and there are seven neighbors within 2.8 Å for both hub atoms. In the panel (b), the blue lines mark stronger bonds along the edge of the cluster [2.48-2.57 Å, bond strength 0.52-0.61], while the green lines mark weaker bonds across it [2.78-2.89 Å, bond strength 0.22-0.28]. The three non-marked bonds in the sheet are in between. The corresponding bonds are also marked with same colors in the c-Ga visualization, although they do not have the same bond distance ordering there. In c-Ga, the nearest-neighbors are Ga_2 dimers with 2.49 Å bond length, and the dimer partner atoms of hub atoms (red dots) are marked with white dots in the visualization.

The cluster in AD structure is broken down during the melt-quench, but in the MQ structure another cluster emerges, which – while still bearing the some visual resemblance – is much more distorted. This cluster has two similar hub atoms, which are 2.78 Å apart, and the visualization is shown in figure 28(c). The bond lengths are longer in the MQ cluster, but the geometry is similar to the cluster in AD structure if the bonds up to 3.03 Å are drawn. Both hub atoms have six neighbors within this radius. It is also notable that the bonds drawn in black in figure 28(c) are all 3.03±0.005 Å long, and their length is below the $r^{\mathrm{min}}_{\mathrm{Ga-Ga}}$ distance of GaSb. The atoms in the MQ cluster were initially tetrahedrally coordinated in the AD structure, which means that there should be no memory effect involved.

The bond angles of GaSb are shown in figure 29, and they peak near the tetrahedral reference angle (109.5°) or slightly below it around 98°. This is also

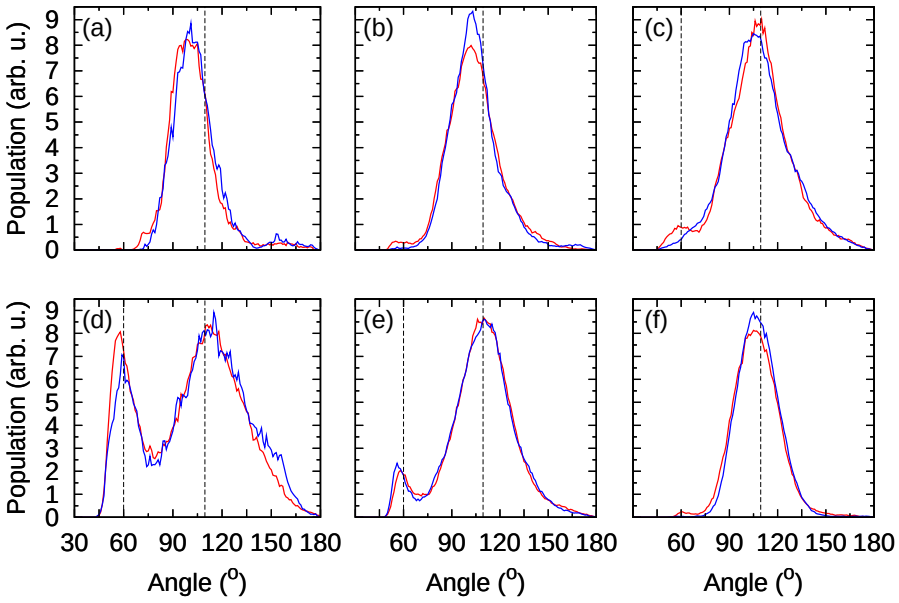

Figure 29: Bond angle distributions in GaSb for (a) Sb-Sb-Sb, (b) Ga-Sb-Sb, (c), Ga-Sb-Ga, (d) Ga-Ga-Ga (e), Ga-Ga-Sb and (f) Sb-Ga-Sb bonds (cutoff 3.2 Å). Red: AD, blue: MQ. Dashed vertical lines at tetrahedral angle (109.5°) and (c-e) 60°.

consistent with fourfold coordination seen from the coordination numbers. There is another peak at 60°, which comes from three-membered rings, triangles, that are present in the structures. The triangles can form clusters, such as a rhombus of four atoms, or bigger clusters as discussed earlier.

The $GaSb_7$ bond angles are shown in figure 30. The antimony-centered bond angle distributions peak at ~98°, which is between the octahedral and tetrahedral reference angles. This is consistent with the distorted octahedral coordination, while the gallium-centered distributions peak at the tetrahedral angle of fourfold coordination. There are very few Ga-Ga-Ga triplets, which means very low statistics for that bond angle distribution. There is some weight near 60°, which indicates the presence of triangular atomic arrangements in the structures, albeit in lower numbers than what was present in GaSb. In addition, the weight of these diminishes significantly from AD to MQ, and they are possibly not intrinsic for the amorphous $GaSb_7$ structure.

5.4.2 Rings and cavities

The ring size distributions of all four structures are shown in figure 31. It shows the existence of the three-membered rings that were evident from the bond angle graph. It also shows that the ring size of GaSb has an upper bound at eight atoms, which means that GaSb does not contain large cavities that large rings could encase. The cavities occupy 22% (AD) and 20% (MQ) of the volume, but in the AD structure there are more cavity domains than in MQ, which indicates different surface-to-volume ratio. The most common rings are rings with five and six atoms, and the numbers of those increase when going from AD to MQ.

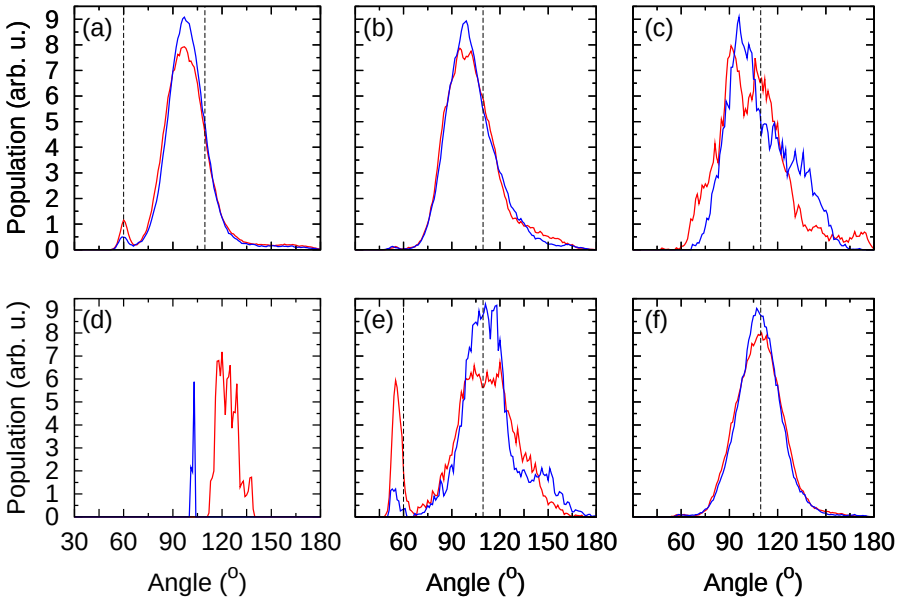

Figure 30: Bond angle distributions in $GaSb_7$ for (a) Sb-Sb-Sb, (b) Ga-Sb-Sb, (c), Ga-Sb-Ga, (d) Ga-Ga-Ga (e), Ga-Ga-Sb and (f) Sb-Ga-Sb bonds (cutoff 3.2 Å). Red: AD, blue: MQ. Dashed vertical lines at tetrahedral angle (109.5°) and (c-e) 60°.

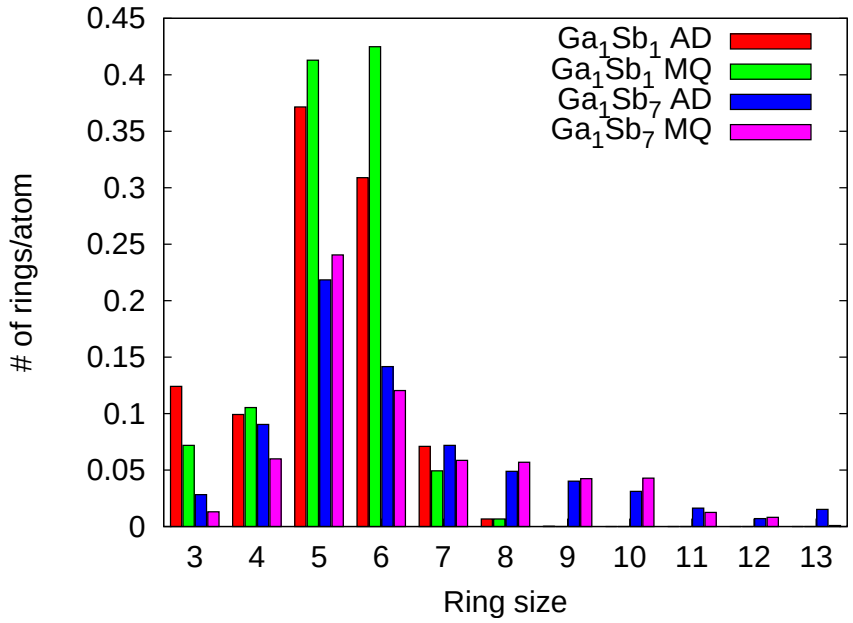

Figure 31: Ring sizes in amorphous GaSb and $GaSb_7$. The bond cutoff is 3.2 Å.

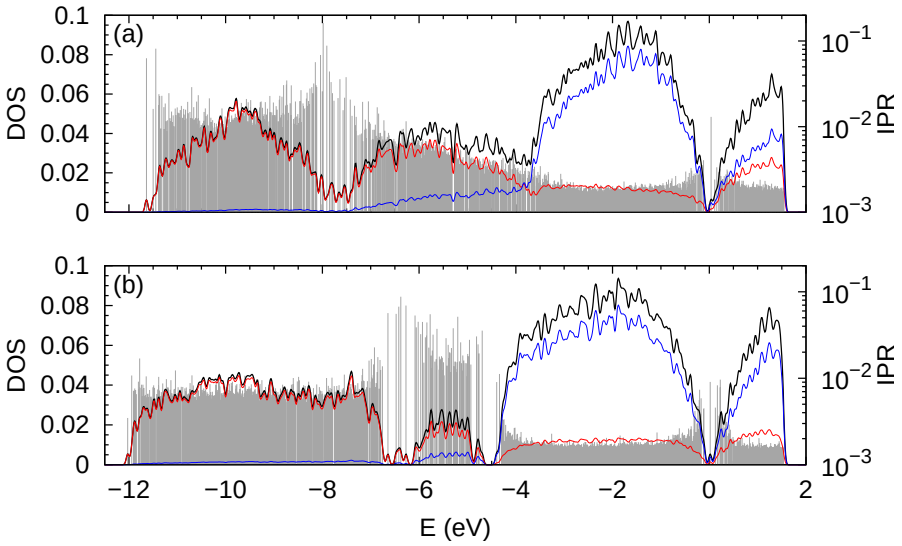

Figure 32: Electronic density of states (DOS, black) of MQ (a) GaSb and (b) $GaSb_7$. Red: *s*-component, blue: *p*-component. The inverse participation ratio (IPR, right scale) is marked in grey.

The ring size distribution of $GaSb_7$ shows that there are very little three-membered rings when compared to GaSb, and their number further decreases from AD to MQ. In general, the difference between $GaSb_7$ AD and MQ structures is less than the corresponding difference in GaSb. The ring distribution peaks at five-membered rings and unlike GaSb, $GaSb_7$ contains large rings. This indicates that there are a number of larger cavities in $GaSb_7$. The total cavity volume of $GaSb_7$ is 24% (AD) and 22% (MQ), which is close to that of GaSb, and the differences between the two compositions are likely to be in the shapes and sizes of the individual cavities. The relative volume of cavity domains in $GaSb_7$ indicate that the surface-to-volume ratio is higher in AD than in MQ, similarly to GaSb.

In the simulations, there are some signs of the segregation mentioned in section 4.5. There exists gallium-free domains in both AD and MQ structures of $GaSb_7$. Over half of the antimony atoms (61-62%) do not bond to gallium, and these atoms form gallium-free regions (i.e. pure elemental antimony), which are of the order of 1 nm across. These are probably too small to cause the two-stage crystallization reported in ref. [73], and it is possible that much larger simulation cells are needed in order to model segregation correctly.

5.4.3 Electronic density of states

The electronic density of states (DOS) and inverse participation ratio (IPR) are shown in figure 32 for the MQ structures of GaSb and $GaSb_7$. IPR is defined as

$$\mathrm{IPR} = \frac{\int \left|\psi(\mathbf{r})\right|^4 \mathrm{d}\mathbf{r}}{\left(\int \left|\psi(\mathbf{r})\right|^2 \mathrm{d}\mathbf{r}\right)^2} \tag{49}$$

and varies from 1 of the fully localized states to $1/N_{\text{states}}$ of the fully delocalized states. The different chemical compositions induce differences in the two *s*-bands and the inverse participation ratio (IPR). In particular the intermediate band near -6 eV is much narrower and more localized in $GaSb_7$, while the lowest band is slightly wider and less localized. The lowest band is associated with Sb, the intermediate band is mixed with mostly Ga in GaSb and mostly Sb in $GaSb_7$. The valence band is associated mostly with Sb in both compositions. Band gaps (GaSb: 0.15 eV, $GaSb_7$: 0.13 eV) most likely underestimate the optical gaps, which is typical for DF calculations. The states near energy gaps are more localized than the others.

5.4.4 Conclusions

We have simulated the GaSb and $GaSb_7$ phase-change materials by creating model structures for as-deposited and melt-quenched amorphous structures of both compositions. The models have 528 atoms each, and they were formed by sequential deposition of sparse layers of atoms on top of a fixed template at 300 K. These film structures were then compressing to the bulk density to create a model for the AD structure. The AD structure was then heated above the melting temperature and quenched to produce the model for the MQ structure.

GaSb prefers tetrahedral coordination, whereas in $GaSb_7$ gallium is tetrahedrally coordinated but antimony has a defective octahedral coordination. In $GaSb_7$, almost half of the fourfold coordinated antimony are weakly bonded to gallium, which enables antimony to have the fourth bonded neighbor. Both materials have many five and six-membered rings and some three-membered rings, but the last are quite rare in $GaSb_7$. The computational total PDF (with XRD weights) agrees well with the experimental PDF measured with XRD by Shevchik and Paul [85].

In GaSb there are no rings with more than eight atoms, which indicates absence of large cavities. In contrast, $GaSb_7$ has larger rings, albeit in low numbers. Cavities make up 20-24% of the total volume in both materials, and in both compositions the surface-to-volume ratio of the cavities is higher in AD than in MQ. We also found small clusters in the GaSb structures, which resemble crystalline gallium. The cluster in AD GaSb was more similar to c-Ga than the one in MQ GaSb, as the cluster in MQ GaSb had more elongated bonds.

In GaSb, gallium and antimony atoms become more interconnected as the structure is melt-quenched, which does not support elemental segregation. Segregation seems to be possible for the $GaSb_7$, where volumes of elemental antimony are present in both AD and MQ structures, and these volumes are approximately 1 nm across. However, proper atomistic studies of phase-separation would require samples much larger than used here, and they would be thus enormously demanding computationally.

6 Summary and outlook

This thesis reports results of computer simulations of phase-change (PC) materials at atomistic level. PC materials have been used in commercial optical rewritable disks (CD, DVD, Blu-ray Disc) and are a potential class of materials for the next-generation electric memory (PC-RAM, PRAM). In particular, PC materials show better cyclability and switching speed than the current Flash memory.

The results include an improved structural model for the amorphous $Ge_{15}Te_{85}$ alloy (prototype PC material) with Ge-Ge bonds playing an important role. The present model encompasses good fit to the experimental data and low total energy according to the density functional energy. It also shows two significantly different local environments for germanium atoms (tetrahedral vs. octahedral), and two different classes of tellurium atoms where bonding with Ge was either present or not.

The crystallization simulations of $Ge_2Sb_2Te_5$ revealed that, at least for the simulation cell sizes attainable with today's supercomputers, percolation of the crystalline cluster starts very early in the crystallization process. Cavities in the structure seem to provide space for the atomic rearrangements, even after the structure is mostly crystallized. Wrong bonds (Ge-Ge, Ge-Sb, Sb-Sb and Te-Te) are present in the structure due to the rapid phase transition with does not support a full relaxation. The simulations agree with the experimental result of 670 K as the fastest crystallization temperature [52].

The computer-aided deposition of Ga/Sb alloys shows that there is little difference in the amorphous AD and MQ structures of GaSb. This agrees with the experimental result of the near-equal crystallization times for the two. However, $GaSb_7$ shows different crystallization times for AD and MQ structures in experiments, but no clear reason for this was found in this study. GaSb was found to lack large ring sizes (N>8) completely, and this was attributed to cavity shapes, while in $GaSb_7$ large rings existed. Initial signs of segregation were found in the $GaSb_7$ alloy, but the small simulation cell sets severe restrictions for studying this effect further.

In general, computational modeling can support experimental work but not to replace it. The computer speed has increased by a factor of $\sim 10^3$ within the last 10 years, and expected to reach an EFLOPS (10^{18} floating point operations per second) performance level in just a few years. In future, it will be possible to calculate structural models with more detail and larger simulation cells. However, the models of atomistic structures are still models, and they need to be verified by experiments. The models give theoretical insight of the important properties and can be used for making predictions, for example of new PC material compositions, and one does not need to test every composition with experiments. Modeling can be used to unravel the atomic structure of amorphous materials as the experiments can only measure averaged quantities (e.g. $S(Q)$, PDF, EXAFS spectra) of these materials. This means that the experimental results cannot be pinpointed to a specific atom, but these results can be used in computer simulations to find out what are the possible structures and atomic arrangements corresponding to the results.

This is even more vital when the disordered structure is changing very rapidly,

as is the case in nanosecond timescale crystallization of PC materials. Here the computer modeling allows to track a (modeled) trajectory of a single atom, which can help to understand how it is possible to form an ordered lattice structure in such a short time. Insights of the atomic movement during crystallization can then help in engineering desired properties for new PC materials.

References

[1] M. Hilbert and P. López, *The world's Technological Capacity to Store, Communicate, and Compute Information*, Science **332**, 60-65 (2011).

[2] C. J. Byrne, M. Eldrup, *Bulk Metallic Glasses*, Science **321**, 502-503 (2008).

[3] E. D. Zanotto, *Do cathedral glasses flow?*, Am. J. Phys. **66**, 392-395 (1998).

[4] L. Berthier and G. Biroli, *Theoretical perspective on the glass transition and amorphous materials*, Rev. Mod. Phys. **83**, 587-645 (2011).

[5] R. O. Jones in *Strongly Correlated Systems*, pp. 1-28. Ed. A. Avella and F. Mancini, Berlin: Springer-Verlag, 2012. ISBN: 978-3-642-21831-6

[6] E. Schrödinger, *Quantisierung als Eigenwertproblem*, Ann. d Physik (Leipzig) **79**, 361-376 (1926).

[7] E. Schrödinger, *An Undulatory Theory of the Mechanics of Atoms and Molecules*, Phys. Rev. **28**, 1049-1070 (1926).

[8] P. A. M. Dirac, *Quantum Mechanics of Many-Electron Systems*, P. R. Soc. A **123**, 714-733 (1929).

[9] J. Kohanoff, *Electronic Structure Calculations for Solids and Molecules*, Cambridge University Press (2006).

[10] L. H. Thomas, *The calculation of atomic fields*, Proc. Cambridge Phil. Soc. **23**, 542-548 (1927).

[11] E. Fermi, *Un Metodo Statistico per la Determinazione di alcune Prioprietà dell'Atomo*, Rend. Accad. Naz. Lincei **6**, 602-607 (1927).

[12] P. A. M. Dirac, *Note on Exchange Phenomena in the Thomas Atom*, P. Camb. Philos. Soc **26**, 376-385 (1930).

[13] K. Capelle, *A Bird's-Eye view of Density-Functional Theory*, Brazilian Journal of Physics **36**, 1318-1343 (2006).

[14] R. O. Jones and O. Gunnarsson, *The density functional formalism, its applications and prospects*, Reviews of Modern Physics **61**, 689-746 (1989).

[15] P. Hohenberg and W. Kohn, *Inhomogeneous Electron Gas*, Phys. Rev. **136**, B864-B871 (1964).

[16] M. Levy, *Universal variational functionals of electron densities, first-order density matrices, and natural spin-orbitals and solution of the v-representability problem*, Proc. Natl. Acad. Sci. USA **76**, 6062-6065 (1979).

[17] T. L. Gilbert, *Hohenberg-Kohn theorem for nonlocal external potentials*, Phys. Rev. B **12**, 2111-2120 (1975).

[18] J. E. Harriman, *Orthonormal orbitals for the representation of an arbitrary density*, Phys. Rev. A **24**, 680-682 (1981).

[19] W. Kohn and L.-J. Sham, *Self-Consistent Equations Including Exchange and Correlation Effects*, Phys. Rev **140**, A1133-A1138 (1965).

[20] B. Civarelli, D. Presti, R. Dovesi and A. Savin, *On choosing the best density functional approximation*, Chem. Modell **9**, 168-185 (2012).

[21] J. P. Perdew and K. Schmidt, *Jacob's ladder of density functional approximations for the exchange-correlation energy*, AIP Conf. Proc. **577**, 1-20 (2001).

[22] J. P. Perdew, K Burke and M Ehrzerhof, *Generalized Gradient Approximation Made Simple*, Phys. Rev. Lett. **77**, 3865-3868 (1996).

[23] J. P. Perdew, A Ruzsinszky, G. I. Cxonka, O. A. Vydrov, G. E. Scuseria, L. A. Constantin, X. Zhou and K. Burke, *Restoring the Density-Gradient Expansion for Exchange in Solids and Surfaces*, Phys. Rev. Lett. **100**, 136406 (2008).

[24] B. Miehlich, A. Savin, H. Stoll and H. Preuss, *Results obained with the correlation energy density functionals of Becke and Lee, Yang and Parr*, Chem. Phys. Lett. **157**, 200-206 (1989).

[25] A. D. Becke, *Density-functional exchange-energy approximation with correct asymptotic behaviour*, Phys. Rev. A **38**, 3098-3100 (1988).

[26] C. Lee, W. Yang and R. G. Parr, *Development of the Colle-Salvetti correlation-energy formula into a functional of the electron density*, Phys. Rev. B **37**, 785-789 (1988).

[27] J. Tao, J. P. Predew, V. N. Staroverov and G. E. Scuseria, *Climbing the Density Functional Ladder: Nonempirical Meta-Generalized Gradient Approximation Designed for Molecules and Solids*, Phys. Rev. Lett. **91**, 146401 (2003).

[28] A. D. Becke, *Density-functional thermochemistry. III. The role of exact exchange*, J. Chem. Phys. **98**, 5648-5652 (1993).

[29] J. P. Perdew in *Electronic Structure of Solids '91*, p. 11. Ed. P Ziesche and H. Edchrig, Berlin: Akademie Verlag, 1991.

[30] P. J. Stephens, F. J. Devlin, C. F. Chabalowski and M. J. Frisch, *Ab Initio Calculation of Vibracional Absorption and Circular Dichroism Spectra Using Density Functional Force Fields*, J. Phys. Chem. **98**, 11623-11627 (1994).

[31] S. H. Vosko L. Wilk and M. Nusair, *Accurate spin-dependent electron liquid correlation energies for local spin density calculations: a critical analysis*, Can. J. Phys. **58**, 1200-1211 (1980).

[32] J. Heyd, G. E: Scuseria and M. Ernzerhof, *Hybrid functionals based on a screened Coulomb potential*, J. Chem. Phys. **118**, 8207-8215 (2003).

[33] J. P. Perdew, M. Ernzerhof and K. Burke, *Rationale for mixing exact exchange with density functional approximations*, J. Chem. Phys. **105**, 9982-9985 (1996).

[34] N. Troullier and J. L. Martins, *Efficient pseudopotentials for plane-wave calculations*, Phys. Rev. B **43**, 1993-2006 (1991).

[35] L. Kleinman and D. M. Bylander, *Efficacious Form for Model Pseudopotentials*, Phys. Rev. Lett. **48**, 1425-1428 (1982).

[36] CPMD, `https://www.cpmd.org/`, ©IBM Corp 1990-2008, ©MPI für Festkörperforschung Stuttgart 1997-2001.

[37] M. E. Tuckerman and G. J. Martyna, *Undertanding Modern Molecular Dynamics: Techniques and Applications*, J. Phys. Chem. B **104**, 159-178 (2000).

[38] J. Kolafa, *Time-Reversible always Stable Predictor-Corrector Method for Molecular Dynamics of Polarizable Molecules*, J. Comput. Chem. **25**, 335-342 (2004).

[39] R. Car and M. Parrinello, *Unified approach for Molecular Dynamics and Density-Functional Theory*, Phys. Rev. Lett. **55**, 2471-2474 (1985).

[40] M. E. Tuckerman and M. Parrinello, *Integrating the Car-Parrinello equations. I. Basic integration techniques*, J. Chem. Phys. **101**, 1302-1315 (1994).

[41] F. Bloch, *Über die Quantenmechanik der Elektronen in Kristallgittern*, Z. Phys. **52**, 555-560 (1928).

[42] P. Koskinen and O. O. Kit, *Efficient Approach for Simulating Disordered Materials*, Phys. Rev. Lett. **105**, 106401 (2010).

[43] S. Nosé, *A unified formulation of the constant temperature molecular dynamics methods*, J. Chem. Phys. **81**, 511-519 (1984).

[44] W. G. Hoover, *Canonical dynamics: Equilibrium phase-space distributions*, Phys. Rev. A **31**, 1695-1697 (1985).

[45] O. Gereben, P. Jóvári, L. Temleitner and L. Pusztai, *A new version of the RMC++ Reverse Monte Carlo programme, aimed at investigating the structure of covalent glasses*, J. Optoelectron. Adv. Mater. **9**, 3021-3027 (2007).

[46] P. Jóvári, I. Kaban, B. Bureau, A. Wilhelm, P. Lucas, B. Beuneu and D. A. Zajac, *Structures of Te-rich Te-Ge-X (X = I, Se, Ga) glasses*, J. Phys.: Condens. Matter **22**, 404207 (2010).

[47] J. Akola, R. O. Jones, S. Kohara, S. Kimura, K. Kobayashi, M. Takata, T. Matsunaga, R. Kojima and N. Yamada, *Experimentally constrained density-functional calculations of the amorphous structure of the prototypical phase-change material $Ge_2Sb_2Te_5$*, Phys. Rev. B **80**, 020201(R) (2009).

[48] S. Raoux, W. Wełnic and D. Ielmini, *Phase Change Materials and Their Application to Nonvolatile Memories*, Chem. Rev. **110**, 240 (2010).

[49] G. W. Burr, M. J. Breitwisch, M. Franceschini, D. Garetto, K. Gopalakrishnan, B. Jackson, B. Kurdi, C. Lam, L. A. Lastras, A. Padilla, B. Rajendran, S. Raoux and R. S. Shenoy, *Phase change memory technology*, J. Vac. Sci. Technol. B **28**, 223-262 (2010).

[50] C. A. Angell, *Formation of Glasses from Liquids and Biopolymers*, Science **267**, 1924-1935 (1995).

[51] H. Neumann, F. Herwig and W. Hoyer, *The short range order of liquid eutectic A_{III}-Te and A_{IV}-Te alloys*, J. Non-Cryst. Solids **205**, 438-442 (1996).

[52] J. Orava, A. L. Greer, B. Gholipour, D. W. Hewak and C. E. Smith, *Characterization of supercooled liquid $Ge_2Sb_2Te_5$ and its crystallization by ultrafast-heating calorimetry*, Nat. Mat. **11**, 279-283 (2012).

[53] JEDEC DDR3 SDRAM standard JESD79-3E.

[54] D. Loke, T. H. Lee, W. J. Wang, L. P. Shi, R. Zhao, Y. C. Yeo, T. C. Chong and S. R. Elliott, *Breaking the Speed Limits of Phase-Change Memory*, Science **336**, 1566-1569 (2012).

[55] S. R. Ovshinsky, *Reversible electrical switching phenomena in disordered structures*, Phys.Rev. Lett. **21**, 1450 (1968).

[56] J. Feinlieb, J. de Neufville, S. C. Moss and S. R. Ovshinsky, *Rapid reversible light-induced crystallization of amorphous semiconductors*, Appl. Phys. Lett. **18**, 254 (1971).

[57] N. Yamada, E. Ohno, N. Akahira, K. Nishiuchi, K. Nagata and M Takao, *High Speed Overwritable Phase Change Optical Disk Material*, Jpn. J. Appl. Phys. **26**, 61 (1987).

[58] S. Raoux, H.-Y. Cheng, M. A. Caldwell and H.-S. P. Wong, *Crystallization times of Ge-Te phase change materials as a function of composition*, Appl. Phys. Lett. **95**, 071910 (2009).

[59] P. K. Khulbe, T. Hurst, M. Horie and M. Mansuripur, *Crystallization Behavior of Ge-Doped Eutectic $Sb_{70}Te_{30}$ Films in Optical Disks*, Appl. Opt. **41**, 6220-6229 (2002).

[60] J. Akola, J. Larrucea and R. O. Jones, *Polymorphism in phase-change materials: melt-quenched and as-deposited amorphous structures in $Ge_2Sb_2Te_5$ from density functional calculations*, Phys. Rev. B **83**, 094113 (2011).

[61] M. Chen, K. A. Rubin and R. W. Barton, *Compound materials for reversible, phase-change optical data storage*, Appl. Phys. Lett. **49**, 502-504 (1986).

[62] M. Anbarasu, M. Wimmer, G. Bruns, M. Salinga and M. Wuttig, *Nanosecond threshold switching of $GeTe_6$ cells and their potential as selector devices*, Appl. Phys. Lett. **100**, 143505 (2012).

[63] D. I. Bletskan, *Phase equilibrium in the systems A^{IV}-B^{VI}*, J. Ovonic Res. **1**, 53-60 (2005).

[64] J. Rocca, M. Erazú, M. Fontana and B Arcondo, *Crystallization process on amorphous GeTeSb samples near to eutectic point $Ge_{15}Te_{85}$*, J. Non-Cryst. Solids **355**, 2068-2073 (2009).

[65] J. Akola and R. O. Jones, *Binary Alloys of Ge and Te: Order, Voids and the Eutectic Composition*, Phys. Rev. Lett **100**, 205502 (2008).

[66] J. Akola and R. O. Jones, *Structural phase transitions on the nanoscale: The crucial pattern in the phase-change materials $Ge_2Sb_2Te_5$ and GeTe*, Phys. Rev. B **76**, 235201 (2007).

[67] H.-Y. Cheng, K.-F. Kao, C.-M. Lee and T.-S. Chin, *Characteristics of Ga-Sb-Te Films for Phase-Change Memory*, IEEE Trans. Magn. **43**, 927-929 (2007).

[68] M. Wuttig and N. Yamada, *Phase-change materials for rewritable data storage*, Nat. Mat. **6**, 824-832 (2007).

[69] T. Nonaka, G. Ohbayashi, Y. Toriumi, Y. Mori and H. Hashimoto, *Crystal structure of GeTe and $Ge_2Sb_2Te_5$ meta-stable phase*, Thin Solid Films **370**, 258-261 (2000).

[70] Z. Sun, J. Zhou, R. Ahuja, *Structure of Phase Change Materials for Data Storage*, Phys. Rev. Lett. **96**, 055507 (2006).

[71] H.-Y. Cheng, S. Raoux and J. L. Jordan-Sweet, *The Crystallization Behavior of Ga-Sb Materials as a Function of Composition for Phase Change Random Access Memory*, Proc. Europ.\Phase Change and Ovonic Symposium (E*PCOS 2011, Zürich) 103-109 (2011).

[72] I. G. Greenfield and R. L. Smith, *Gallium-Antimony System*, Trans. Am. Inst. Min. Metall. Pet. Eng. **203**, 351-353 (1955).

[73] S. Raoux, A. K. König, H.-Y. Cheng, D. Garbin, R. W. Cheek, J. L. Jordan-Sweet and M. Wuttig, *Phase transitions in Ga-Sb phase change alloys*, Phys. Status Solidi B **249**, 1999-2004 (2012).

[74] L. van Pieterson, M. H. R. Lankhorst, M. van Schijndel, A. E. T. Kuiper and J. H. J. Roosen, *Phase-change recording materials with a growth-cominated crystallization mechanism: A material overview*, J. Appl. Phys. **97**, 083520 (2005).

[75] J. Akola, R. O. Jones, S. Kohara, T. Usuki and E. Bychkov, *Density variations in liquid tellurium: Roles of rings, chains and cavities*, Phys. Rev. B **81**, 094202 (2010).

[76] J. Akola and R. O. Jones, *Structure and dynamics in amorphous tellurium and Te_n clusters: A density functional study*, Phys. Rev. B **85**, 134103 (2012).

[77] P. Jóvári, I. Kaban, W. Hoyer, R. G. Delaplane and A. Wannberg, *Local atomic environment in amorphous $Ge_{15}Te_{85}$*, J. Phys. Condens. Matter. **17**, 1529-1536 (2005).

[78] I. Kaban, P. Jóvári, W. Hoyer and E. Welter, *Determination of partial pair distribution functions in amorphous $Ge_{15}Te_{85}$ by simultaneous RMC simulation of diffraction and EXAFS data*, J. Non-Cryst. Solids **353**, 2474-2478 (2007).

[79] J. Y. Raty, V. V. Godlevsky, J. P. Gaspard, C. Bichara, M. Bionducci, R. Bellissent, R. Céolin, J. R. Chelikowsky and P. Ghosez, *Local structure of liquid GeTe via neutron scattering and ab initio simulations*, Phys. Rev. Lett. **65**, 115205 (2002).

[80] A. Ioffe and S. Neov, *Precise determination of the neutron scattering length of tellurium* Physica B **234**, 1183-1185 (1997).

[81] C. S. Schneider, *Coherent Nuclear Scattering Amplitudes of Germanium, Copper and Oxygen for Thermal Neutrons* Acta Cryst. A **32**, 375-379 (1976).

[82] T. H. Lee and S. R. Elliott, *Ab Initio Computer Simulation of the Early Stages of Crystallization: Application to $Ge_2Sb_2Te_5$ Phase-Change Materials*, Phys. Rev. Lett. **107**, 145702 (2011).

[83] P. J. Steinhardt, D. J. Nelson and M. Ronchetti, *Bond-orientational order in liquids and glasses*, Phys. Rev. B **28**, 784-805 (1983).

[84] D.-H. Kim, F. Merget, M. Laurenzis, P. H. Bolivar and H. Kurz, *Electrical percolation characteristics of $Ge_2Sb_2Te_5$ and Sn doped $Ge_2Sb_2Te_5$ thin films during amorphous to crystalline phase transition*, J. Appl. Phys. **97**, 083538 (2005).

[85] N. J. Shevchik and W. Paul, *The structure of tetrahedrally coordinated amorphous semiconductors*, J. Non-Cryst. Solids **13**, 1-12 (1973/74).

[86] B. D. Sharma and J. Donohue, *A refinement of the crystal structure of gallium.*, Z. Kristallogr. **117**, 293-300 (1962).

[87] T. Matsunaga, J. Akola, S. Kohara, T. Honma, K. Kobayashi, E. Ikenaga, R. O. Jones, N. Yamada, M. Takata and R. Kojima, *From local structure to nanosecond recrystallization dynamics in AgInSbTe phase-change materials*, Nat. Mat. **10** 129-134 (2011).